Thermal Instability in the Manufacturing of Wind Turbine Blade Spar Caps

Author: Nathan Sharp
Rebecca Cutting
Drew Sommer
Date: June 16, 2020

Final Technical Report
IACMI/R000-2020/7.2

Approved for Public Release.
Distribution is Unlimited.

THE COMPOSITES INSTITUTE

U.S. DEPARTMENT OF ENERGY

The information, data, or work presented herein was funded in part by the Office of Energy Efficiency and Renewable Energy (EERE), U.S. Department of Energy, under Award DE-EE0006926

Thermal Instability in the Manufacturing of Wind Turbine Blade Spar Caps

Principal Investigator: Nathan Sharp

Organization: Purdue University – Composites Manufacturing and Simulation Center

Address: 1105 Challenger Ave, Suite 100, West Lafayette, IN 47906

Phone:

Email: nsharp@purdue.edu

Co-authors:

- Rebecca Cutting, Purdue University College of Engineering, Composites Manufacturing and Simulation Center, West Lafayette, Indiana, 47906
- Drew Sommer, Purdue University College of Engineering, Composites Manufacturing and Simulation Center, West Lafayette, Indiana, 47906

Date Published: (January, 2020)

Prepared by:
Institute for Advanced Composites Manufacturing Innovation
Knoxville, TN 37932
Managed by Collaborative Composite Solutions, Inc.
For the
U.S. DEPARTMENT OF ENERGY
Under contract DE- EE0006926

Project Period:
(05/2019 – 12/2019)

TABLE OF CONTENTS

1. LISTS

1.1 List of Acronyms

CMSC – Composites Manufacturing and Simulation Center
DIC – Digital image correlation
DSC – Differential scanning calorimeter
HAWT – Horizontal axis wind turbine
LCOE – Levelized cost of energy
NCF – Non-crimp fabric
VARTM – Vacuum assisted resin transfer molding

1.2 List of Figures

1.2 List of Tables

2. EXECUTIVE SUMMARY

As wind turbine blades continue to scale in length and total mass, the acceptability of traditional approaches for the engineering of processes to build these products has reached a limit. The continued need to reduce the levelized cost of energy (LCOE) drives manufacturing cycle times lower and the net mass of critical components challenges even the most experienced fabricators to meet the quality requirements for safe operating performance over the 25-year design life of the blade. In trying to reduce cycle time for key components of wind turbines, manufacturers discovered occasional buckling of fibers in wind turbine blade spar caps. The cause of the buckling was unknown. The goal of this project was to show that a comprehensive simulation, which considered all of the physics of the VARTM process, could identify the cause of the fiber buckling in spar caps that has been observed during the manufacturing process. Ultimately, the simulation determined the manufacturing process and parameters could lead to significant compressive stresses in the fibers eventually causing buckling. Simulation results suggest that the stress introduced from friction is the largest source of compressive stress in the fibers, the stress from the weight of gravity is significant but secondary, and the compressive stress from cure shrinkage does not play a significant role in the buckling of fibers. This report provides details of the testing and simulation methodology used to identify the cause of the fiber buckling.

3. INTRODUCTION

This report covers the results of a six-month IACMI project between TPI Composites and Purdue University that had a goal of identifying the root cause of fiber buckling behavior in spar caps which was observed occasionally in the manufacturing process. The project scope included material characterization for the relevant materials and physics as well as development of a model that simulated all of the relevant physics in a spar cap VARTM process. A full understanding of the infusion process, reaction rate, cure kinetics, modulus advancement, and thermal expansion through simulation allowed the identification of process variables (such as layout of infusion feedlines, infusion resin and mold temperature settings) that improve the speed of cure while lessening the possibility of fiber buckling in the reinforcements that lead to scrapped components. Manufacturing cost could be greatly reduced with increased capacity and improved facility utilization.

The final goal was to create a model, which included all relevant physics, that could be used to guide optimal processing conditions for speeding up manufacturing without causing part defects. The strategy was to first experimentally recreate the problem and study it to identify root causes of the thermal waviness defect. Next, models were applied to find optimal processing conditions, and finally, validation experiments were conducted to confirm model predictions. An extensive material characterization required to populate the model was also conducted.

4. BACKGROUND

As wind turbine blades continue to scale in length and total mass the acceptability of traditional approaches for the engineering of processes to build these products has reached a limit. The continued need to reduce the LCOE drives manufacturing cycle times lower and the net mass of critical components challenge even the most experienced fabricators to meet the quality requirements for safe operating performance over the 25-year design life of the blade.

Specifically, the common feature of all upwind horizontal axis wind turbine (HAWT) blades is the large structural beam that spans the length of the blade and limits flapwise deflection (and thus avoids tower strike). Whether the structural beam is in the configuration of an I-beam or box-beam, the flanges of the beam are most often constructed as a double tapered, constant width plate. These flanges are referred to as the turbine blade "spar cap". In this case, the reinforcements of the spar cap are constructed as either glass or carbon plies of knitted unidirectional non-crimp fabrics (NCF's) and laid-up on large molds with heated surfaces that allow conduction of thermal energy. An alternate manufacturing approach using pultrusion is available for the spar cap reinforcements, but was not considered in this work.

The fiber buckling has been observed to occur with elevated cure temperatures. The resin cure time is directly related to temperature, and a need for lower temperatures (to avoid fiber buckling) means the cure time increases. This limits the throughput times for manufacturing spar caps on large scale HAWT blades.

Figure 1 shows an image of a fiber-buckling defect that occurred during manufacturing. A change to the manufacturing process was made to remove the fiber-buckling, but that subsequently increased the cycle time of the part.

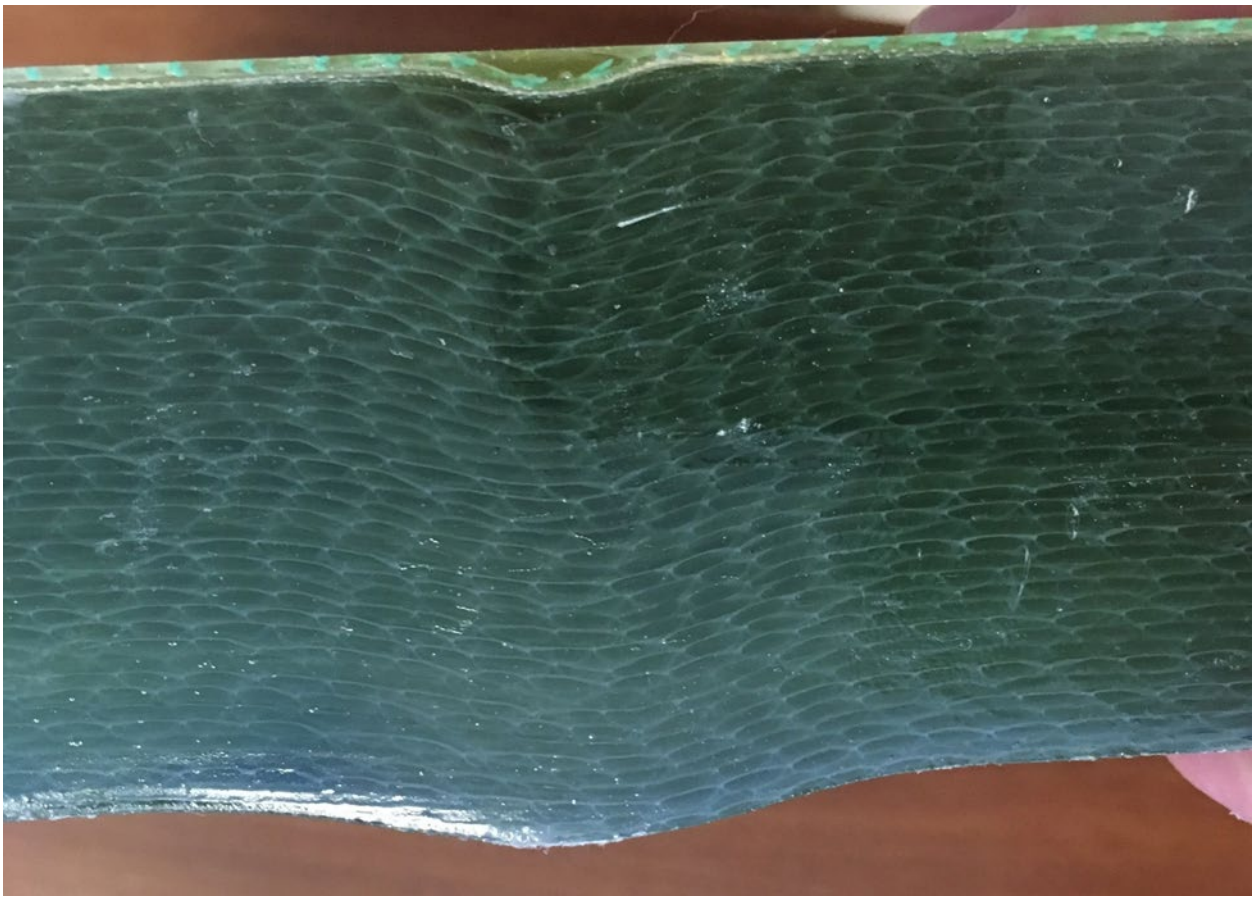

Figure 1: Example of fiber buckling defect that occurs at a cross section along the spar cap at high temperatures

5. RESULTS AND DISCUSSION

5.1 Material Characterization

Material characterization was a necessary step for simulating the manufacturing process of the spar caps. The resin system used was EPIKOTE MGS RIMR 035c and the hardener was Epikure Curing Agent RIMH 038. The material characterization work consisted of measuring material behavior for 100:28 resin (035c) to hardener (RIMH 038) mixture and an Owens Corning 1800 GSM unidirectional stitched glass fabric. The resin properties measured were cure kinetics, viscosity, modulus, and chemical shrinkage. The glass properties measured were modulus and permeability. Fiber volume fraction, modulus, and coefficient of thermal expansion were measured as composite properties. It was found that friction could play a role in the development of compressive stresses and ultimately fiber buckling. Therefore, the friction between the mold and the cured composite was also characterized.

5.1.1 Resin Properties

Cure Kinetics

Experiments with a differential scanning calorimeter (DSC) provided data on the resin system such as the glass transition temperature and crystallization data. For these experiments, a mass ratio of 100:28 was used to mix the resin and hardener (035c Resin + RIMH 038). The mixture was stored in the freezer at -20˚C to delay curing between tests.

The mixture of resin and hardener was placed inside a small aluminum pan, and a press was used to seal the pan shut (ref. Figure 2). An additional empty aluminum pan was used in the analysis as the reference sample. The objective of the experiment is to measure the heat that is absorbed or released from the polymer, however, the metal pan is also affected by temperature change. The use of an empty aluminum container allows for compensation of the results. The empty aluminum pan results provided data for a void container and those are subtracted from the results of interest, and this isolates the polymer data.

Once both containers are sealed, they are placed next to one another in the heating chamber. Figure 3 shows the DSC and the samples that were placed inside. Figure 4 is a diagram of the heating chamber within the DSC.

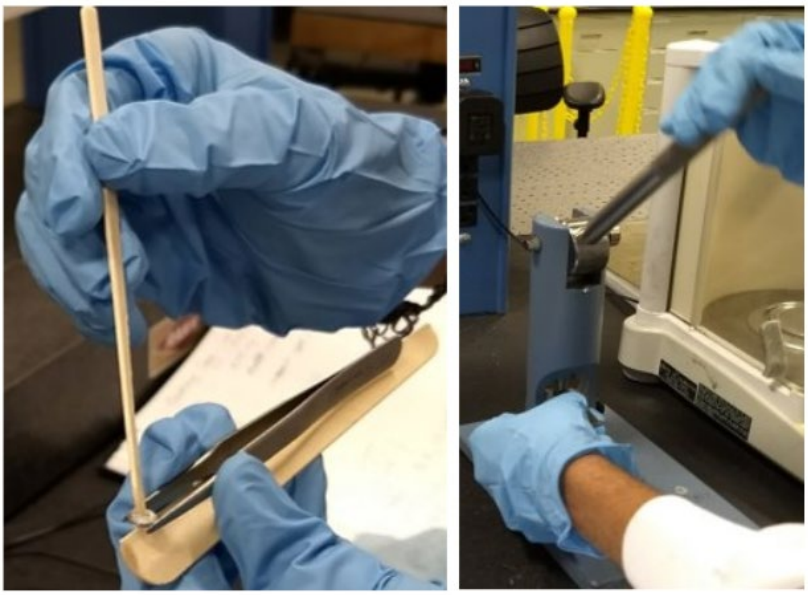

Figure 2: On the left, a sample is placed in the aluminum container with a wooden probe. On the right, the container is crimped closed with the resin inside.

Figure 3: The left shows the inside of the heating chamber containing the two samples. The right image shows the closed chamber with the samples.

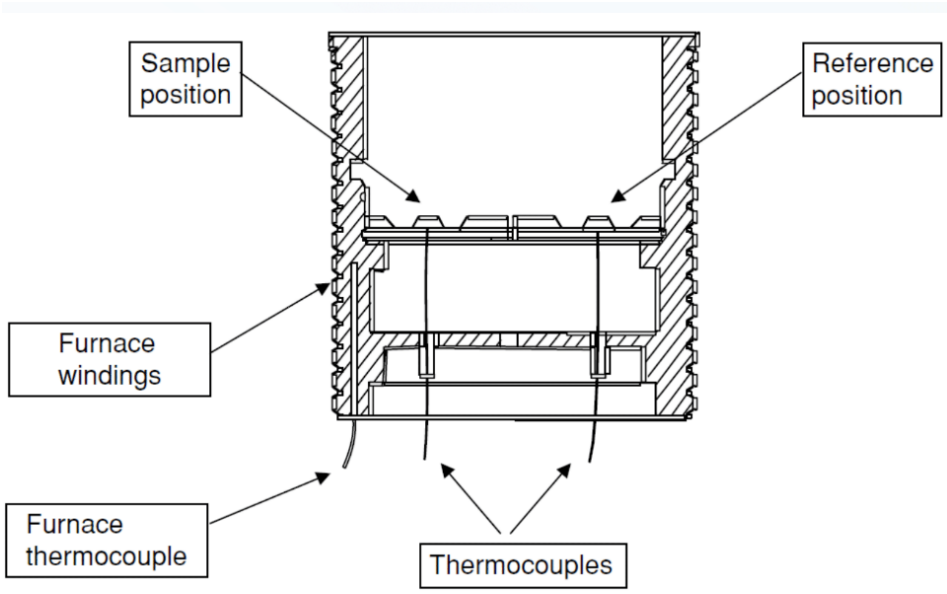

Figure 4: Two samples are placed within the heat chamber of the DSC, and the DSC regulates the temperatures based off the desired inputs.

The DSC ran isothermal experiments at five different temperatures. The different temperatures and corresponding masses of the resin are presented in Table 1. The provided masses are for the resin samples only as the mass of the aluminum pan was subtracted out.

Table 1: The five isothermal test specimens, the temperature in which the tests were performed and the mass of each. (Pan mass= 46.06 mg)

Isothermal Temp (C)	Resin Mass (mg)
50°C	15.0
60°C	15.5
70°C	11.0
80°C	12.1
90°C	10.5

Dynamic tests were also carried out with linearly increasing temperature as a function of time. The ramp rates and masses of each specimen are presented in Table 2.

Table 2: Dynamic tests and their respective ramp rates and masses.

Dynamic Ramps	Mass (mg)
2°C /min	13.0
3°C /min	10.7
5°C /min	15.0

7°C /min	13.0

Figure 5 shows the mass-normalized heat flow results for all samples that were produced from the DSC. Based on the total amount of heat that was generated from these samples, it was determined that the total heat of reaction for this material is roughly 480 J/g. The degree of cure for each sample with respect to time was estimated by integrating the heat flow curves and dividing by the total heat of reaction. Figure 6 shows the results of this operation.

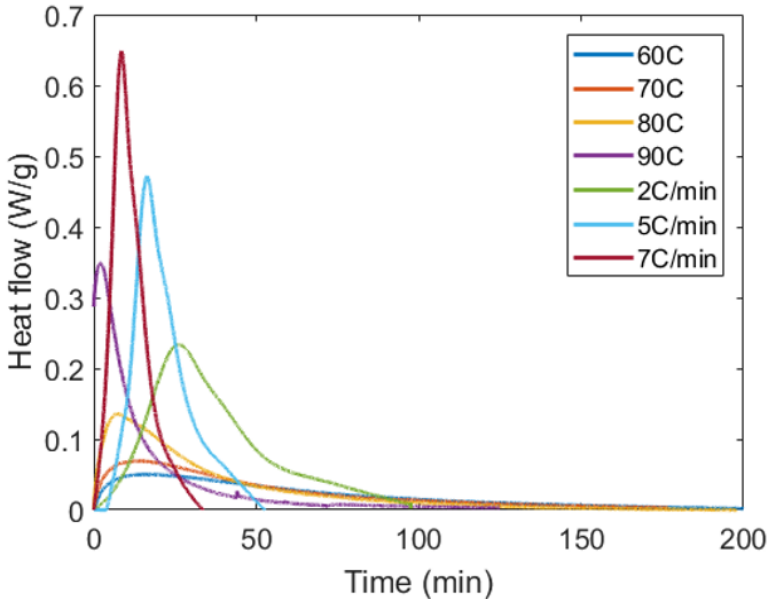

Figure 5: Mass normalized heat flow curves from the DSC

.

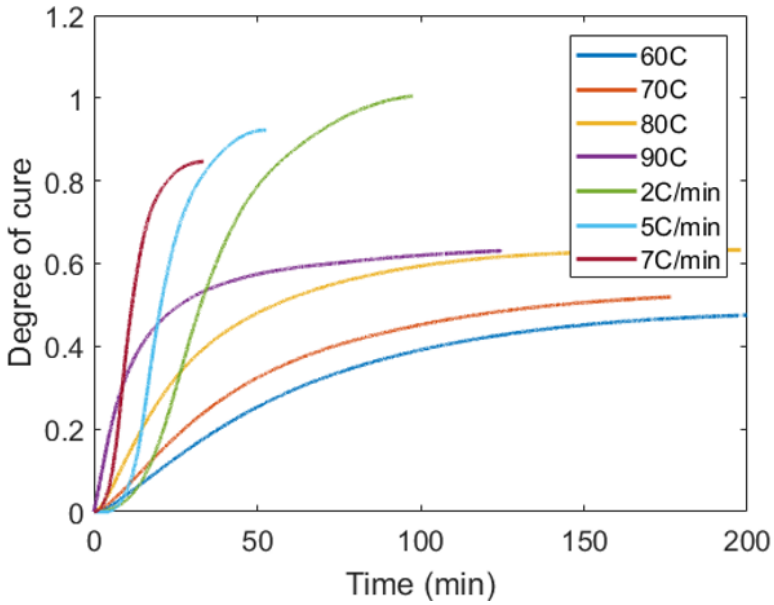

Figure 6: Degree of cure was estimated by integrating the heat flow curves with respect to time and dividing by total heat of reaction.

The desired outcome from this data is a surface which can be queried to estimate the cure rate for the resin given any temperature and state of cure. The heat flow and degree of cure measurements from Figure 5 and Figure 6 were plotted as a function of temperature, degree of cure, and associated cure rate in Figure 7. The desired cure rate surface was generated by fitting a surface to the measured data, as shown in Figure 8. As a check, the fitted surface was used to estimate the cure behavior given the temperature histories recorded in experiment. Figure 9 shows that estimated surface matches the measured response closely.

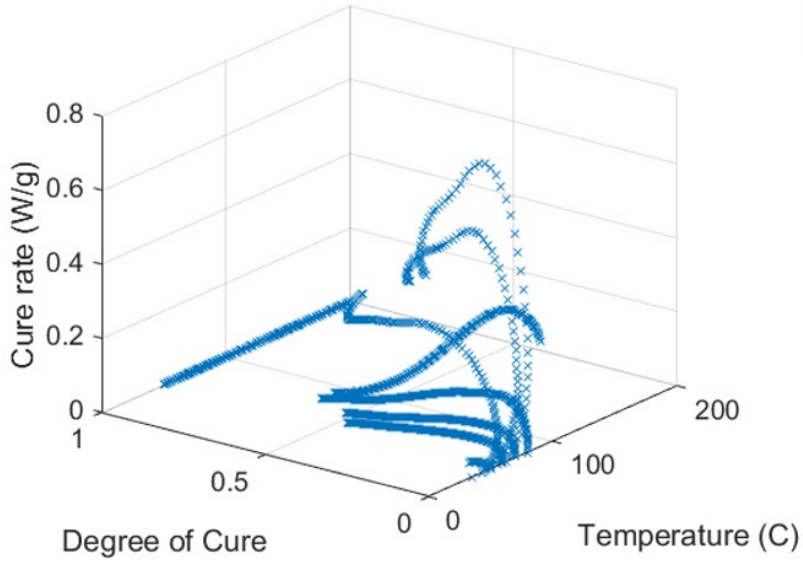

Figure 7: Measured data points plotted with temperature, degree of cure, and cure rate.

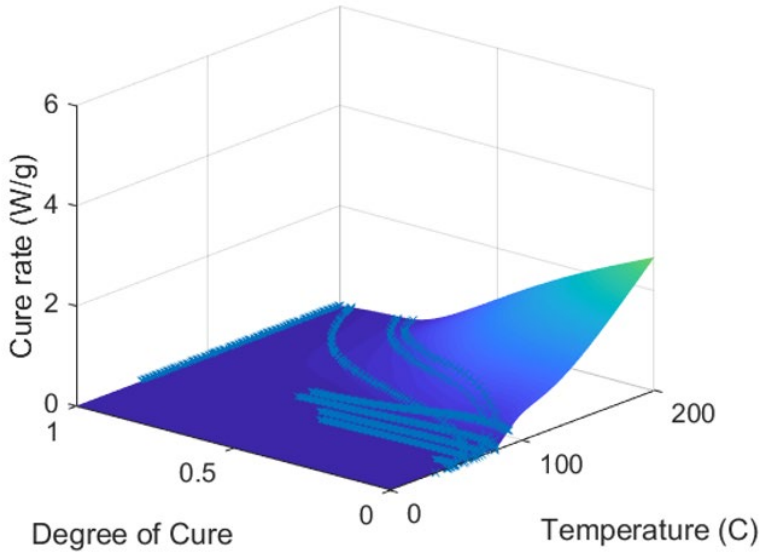

Figure 8: Cure rate surface fit from measured data points.

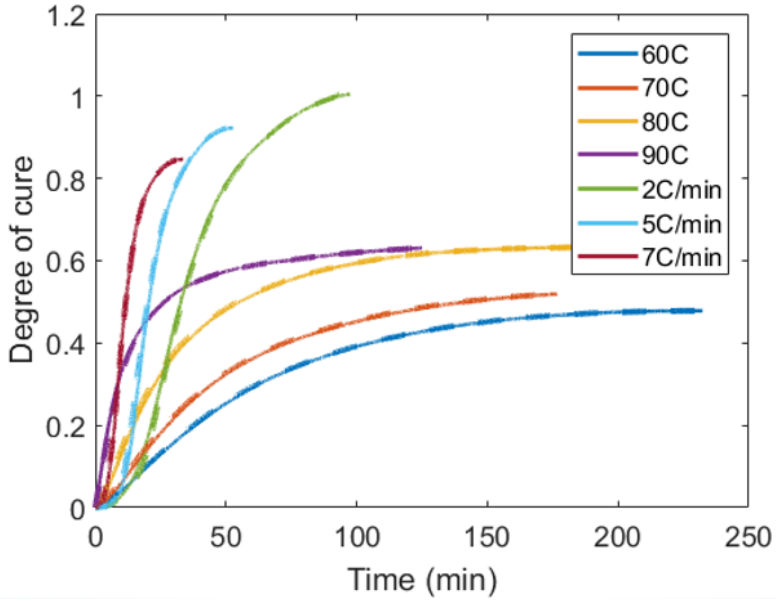

Figure 9: Modeled cure responses match closely with measured responses.

Rheometry

A parallel plate rheometer was used to measure the viscosity, storage modulus, and cure shrinkage of the neat resin. All the tests were completed in strain control mode with 1% strain at 20 rad/sec. Figure 10 shows the rheometer set up.

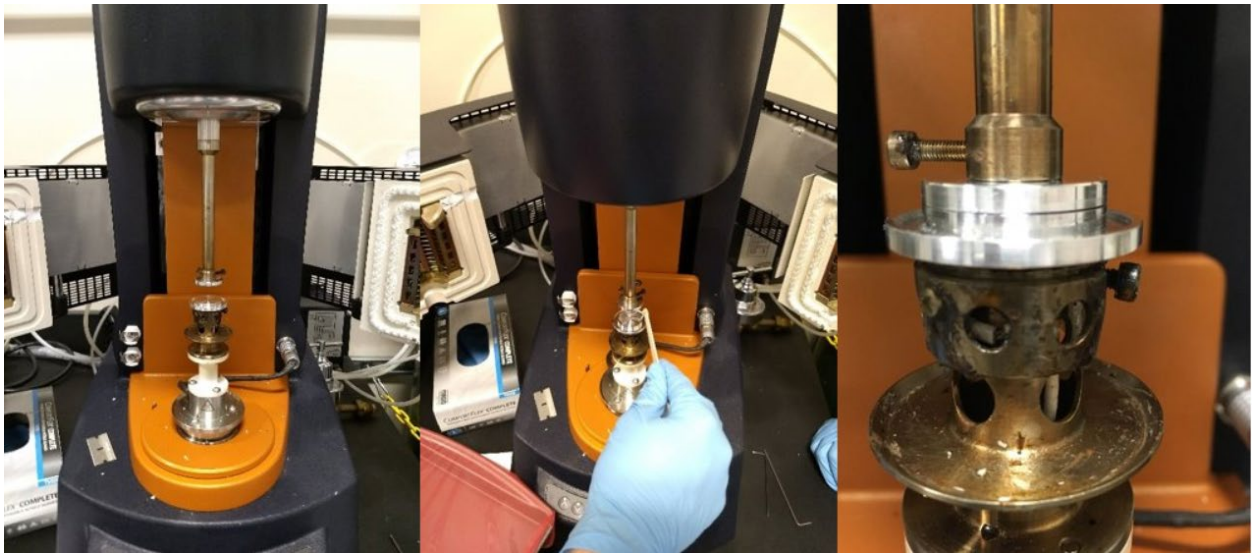

Figure 10: On the left, the rheometer is shown after the gap between the two plates has been recalibrated. In the center, the application of the epoxy resin to the plates. On the right, the plates have been closed with the sample, and the test is ready to begin.

Viscosity

A sampling of the temperature histories used to measure cure kinetics was also used to obtain the viscosity measurements. The previously generated cure rate surface was used to estimate the degree of cure for all samples as a function of time. The viscosity of the resin as a function of temperature and degree of cure was then fit to a Castro-Macosko model (Castro & Macosko, 1982):

$$\mu(T,\alpha) = \mu_0 exp\left(\frac{E}{T}\right)\left(\frac{\alpha_g}{\alpha_g - \alpha}\right)^{(C_1 + C_2\alpha)},$$

where is viscosity, is temperature, is degree of cure, is the degree of cure at gelation, and the other variables are fitting parameters for the model. Figure 11 shows the measured viscosity compared to results of the fitted Castro-Macosko model. Table 3 shows the model parameters.

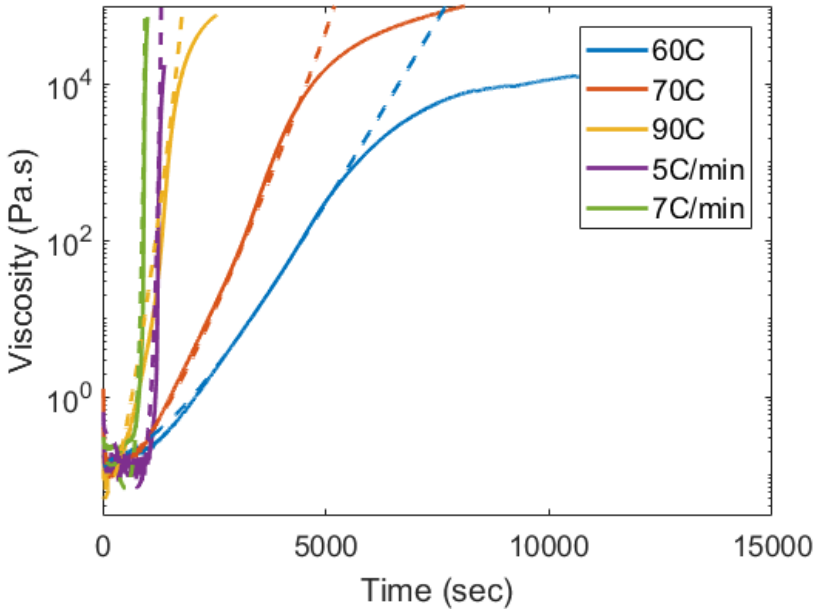

Figure 11: Comparison between measured and modeled resin viscosity.

Table 3: Castro-Macosko model parameters.

Parameter	Value
μ_0	2.7e-7
E	4.4e3
α_g	0.395
C_1	3.2
C_2	8.8

Storage Modulus

The modulus of the resin as a function of temperature and degree of cure was estimated by generating the temperature dependent modulus of the cured resin. Figure 12 shows the measured modulus of the cured resin as a function of temperature.

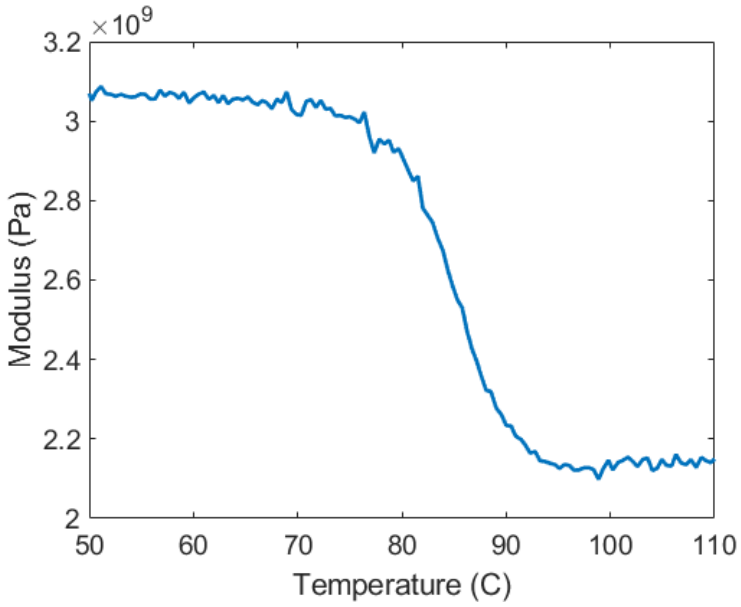

Figure 12: Temperature dependent modulus of the cured resin.

The modulus was fit to the following piecewise linear function:

$$E_{r,cured} = \begin{cases} E_{max}, & T < T_a \\ E_{max} - (E_{max} - E_{min})\left(\frac{T - T_a}{T_b - T_a}\right), & T_a < T < T_b \\ E_{min}, & T_b < T \end{cases}$$

The parameters for this function are listed in Table 4.

Table 4: Cured temperature dependent resin modulus function parameters.

Parameter	Value
E_{max}	3.08 GPa
E_{min}	2.14 GPa
T_a	77 C
T_b	92 C

The modulus of the resin was also modeled as a function of degree of cure by using the storage modulus measurements of the resin from the same runs that were used to model viscosity. Figure 13 shows the storage modulus measurements.

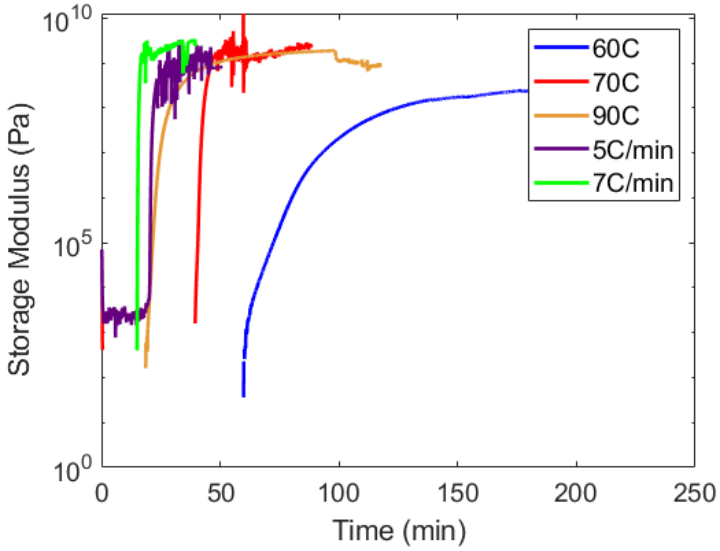

Figure 13: Storage modulus measurements.

The modulus of the resin as a function of temperature and degree of cure was fitted using a form of a Dibenedetto equation (DiBenedetto, 1987):

$$E_r = E_{r,cured}\left(\frac{\lambda\left(\frac{\alpha-\alpha_g}{1-\alpha_g}\right)}{1-(1-\lambda)\left(\frac{\alpha-\alpha_g}{1-\alpha_g}\right)}\right)$$

The gel point, , was found in the viscosity modeling, shown in Table 3. The only other fitting parameter, , was found to be 0.5. Figure 14**.** shows that the Dibenedetto model compares well with the experimental results.

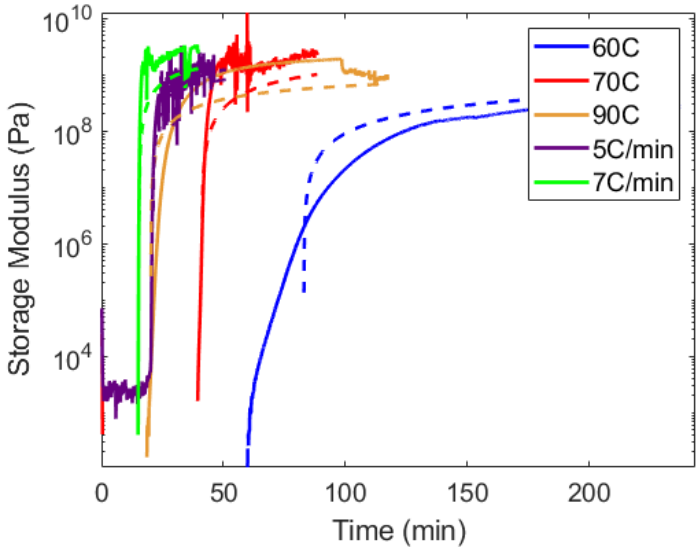

Figure 14: Comparison of measured modulus to modeled modulus.

Cure Shrinkage

The cure shrinkage was measured with the rheometer using the axial force results from testing. As the resin cures, it shrinks causing a tensile force on the rheometer fixture. This tensile force is measured during testing and can be used to predict cure shrinkage. Using the previously modeled cure kinetics and modulus of the resin as a function of temperature and degree of cure, the axial force on the rheometer fixture can be predicted as a function of cure shrinkage. Figure 15 shows the axial force measured for a sample that was cured at 90 C, as well as the predicted force with a cure shrinkage of 0.033. Note that this is a linear shrinkage, so the volumetric shrinkage for this material will be equal to 0.099.

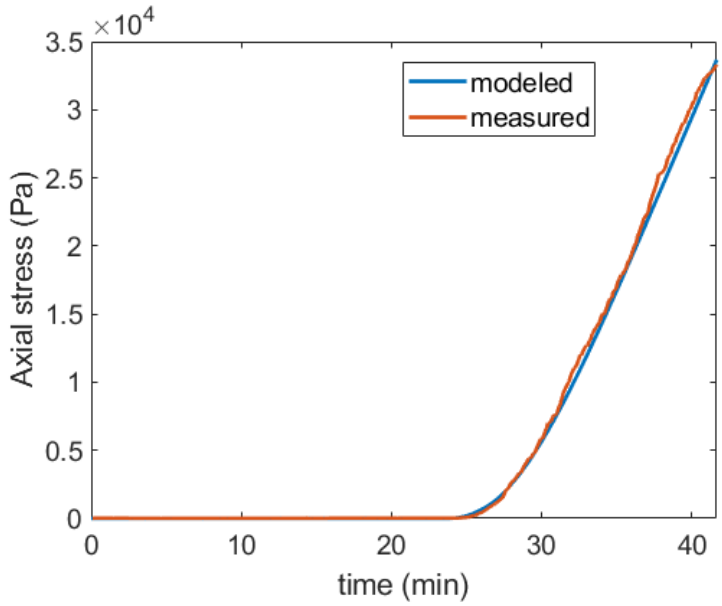

Figure 15: Axial force on the rheometer fixture is used to back out cure shrinkage properties.

5.1.2. Glass Properties

Permeability

Permeability is a measure of how easily a liquid can flow through a porous material such as a glass fiber fabric. Permeability is strongly dependent on fiber volume fraction, and pressure on the fabric. Therefore, the first step in measuring permeability is to run a fiber bed compaction test to evaluate the compression needed to be comparable to the 1 atmosphere of pressure that is applied to the fabric during a VARTM process. This test is performed by stacking fabric in a compression fixture of a load cell and measuring the amount the fabric compresses as a function of the applied pressure. Figure 16 shows the resulting pressure versus percent compression curve, and reveals that the permeability should be measured at roughly 20 percent compression.

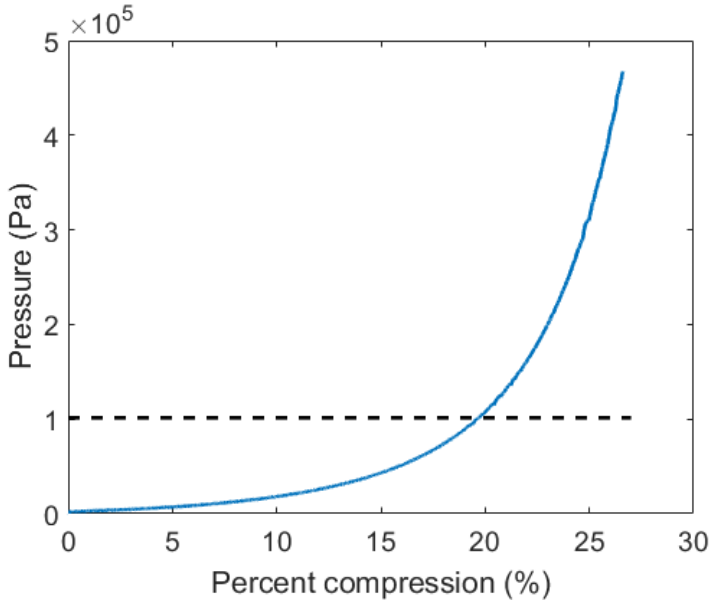

Figure 16: Permeability should be measured at 20% compression for 1 atm.

The in-plane permeability was measured by introducing oil with a known viscosity into the fabric at a specific, measured pressure, and observing the flow front of the oil as a function of time. Permeability can then be backed out using Darcy's Law (Darcy, 1856):

$$K = \frac{v\mu L}{P},$$

where KK is permeability, v is velocity (measured), μ is viscosity (known), L is flow front distance (measured), and P is pressure (fixed). In this case, a motor pumped the oil into the fabric at a specified pressure which was measured with a pressure gage while pictures were taken periodically. Figure 17 shows a series of images showing the advancement of the oil flow front with time. The flow front distances were gathered in the fiber direction and transverse direction in a series of images and plotted to get a least squares solution for the in-plane permeabilities, as shown in Figure 18.

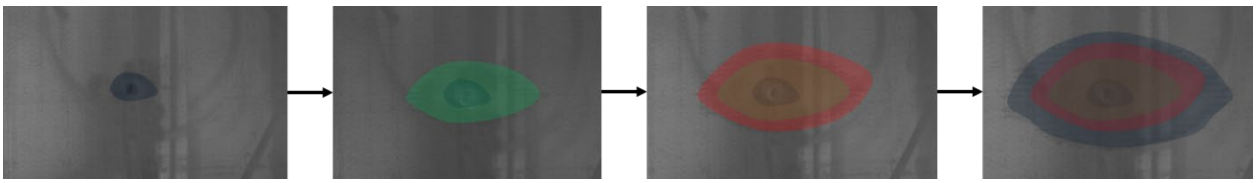

Figure 17: Flow front as a function of time (colors are overlayed for clarification).

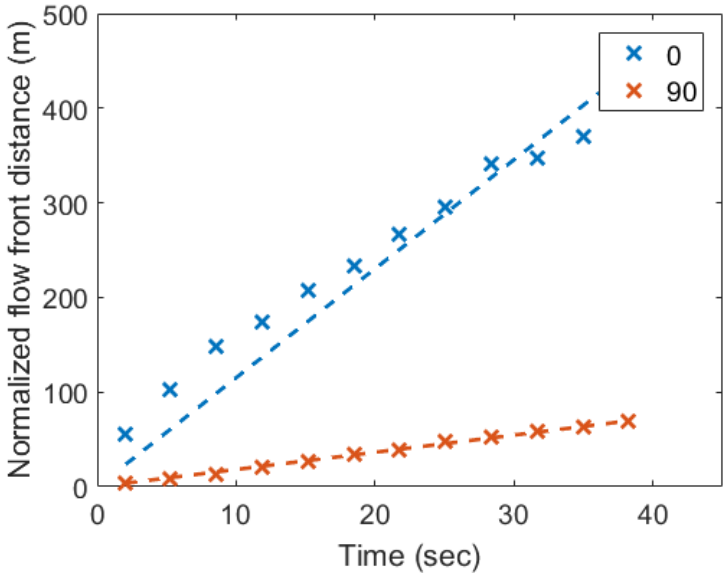

Figure 18: Linear regression used to estimate permeability.

Through thickness permeability cannot be measured in this way; instead, a thick stack of glass fabric (9.5 mm) is placed between the transparent blocks and the time is measured from the start of infusion to when the oil reaches the bottom plate (image shown in Figure 19).

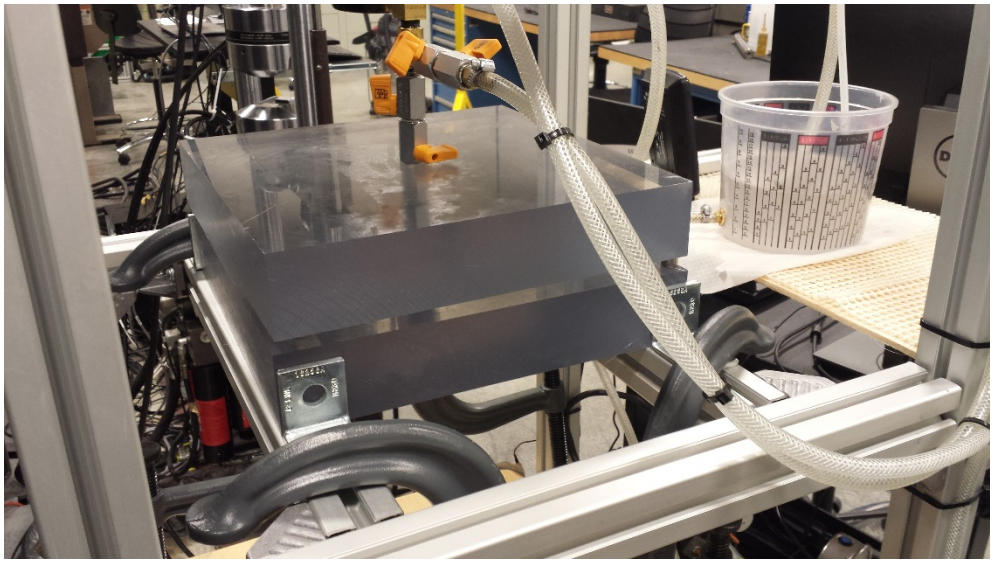

Figure 19: Through thickness permeability setup.

The permeability is then estimated using a derivation from Darcy's Law of the time required for the oil to travel a given distance, *x*, assuming a constant velocity:

$$K = \frac{\mu \Delta x^2}{P \Delta t}$$

This experiment was repeated four times with good agreement. The measured permeability values in all three directions are reported in Table 5, where is the permeability coefficient in the 1 direction (in-plane longitudinal), , is the permeability coefficient in the 2 direction (in-plane transverse), and is the permeability in the 3 direction (through thickness).

Table 5: Measured permeability coefficients

Parameter	Value
k_1	2.77e-10 m^2
k_2	4.37e-11 m^2
k_3	1.30e-14 m^2

5.1.3. Composite Properties

To conduct composite property tests, cured fiberglass composite plates were manufactured. Two 254 mm by 254 mm plates were made through VARTM. Each plate consisted of four 254 mm square plies of glass fibers all aligned in the same direction. A liquid release film was applied to an aluminum base tool. The glass was laid down, followed by a release film, transfer medium and a vacuum bag. The tacky tape was placed near the edges of the glass fibers to impede race tracking (when the resin finds a path to flow that avoids flowing through the fibrous medium). Two hoses were sealed under the vacuum bag to be the vacuum and resin inlet. The inlet hose was clamped and a vacuum was applied to ensure there were no leaks. Afterwards, a secondary vacuum bag was applied on top to help maintain a uniform pressure during infusion. The vacuum was applied via a vacuum port. Figure 20 shows the final set up during infusion. Once infused, it was left for 24 hours to cure at room temperature.

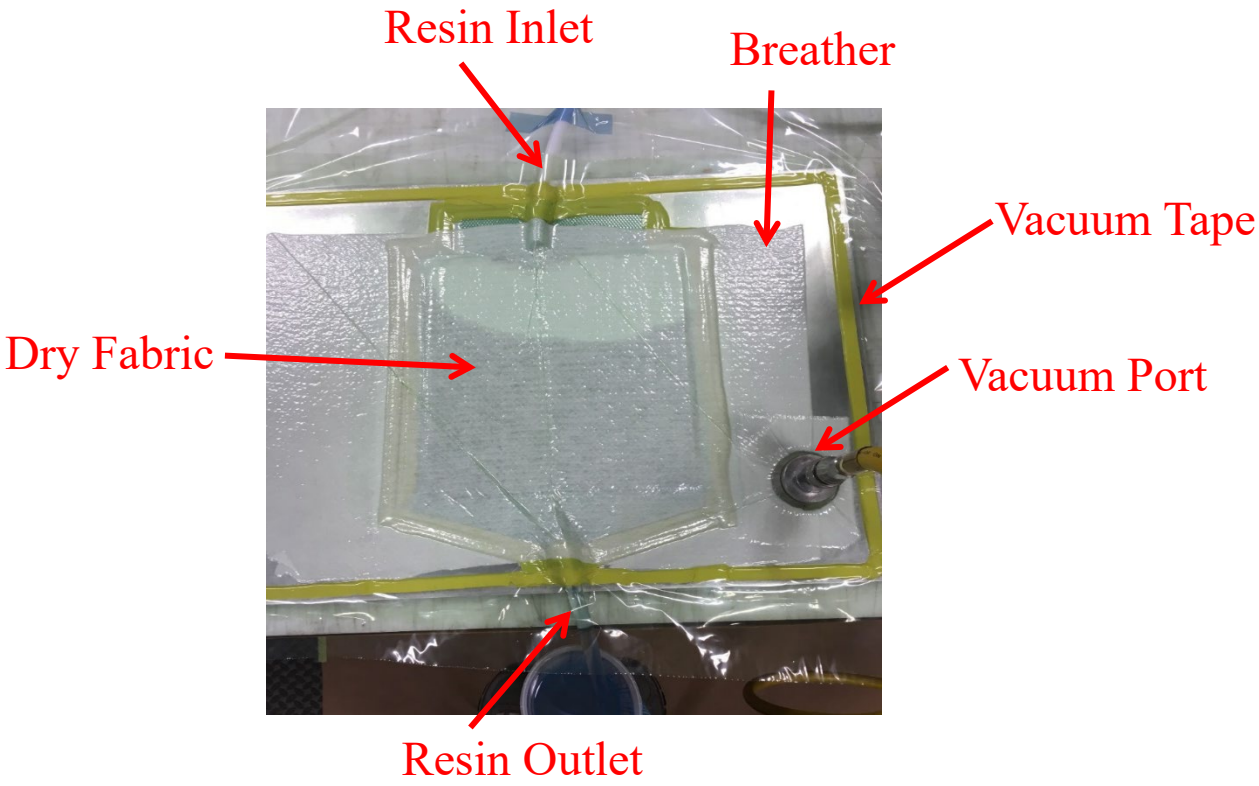

Figure 20: A 254 mm by 254 mm plate was made by infusing 4 plies of glass fibers.

Fiber Volume Fraction

The fiber volume fraction of the composite material was measured by polishing a sample of cured composite with the polished face perpendicular to the fiber direction. All fibers whose center was inside the image were counted and the fiber volume fraction was estimated as:

$$V_f = \frac{N_f \pi \bar{r}_f^{\,2}}{A},$$

where is the fiber volume fraction, is the number of fibers in the image, is the average radius of a fiber, and is the image area. Figure 21 shows an image of this process; the estimated fiber volume fraction for this composite is 0.54.

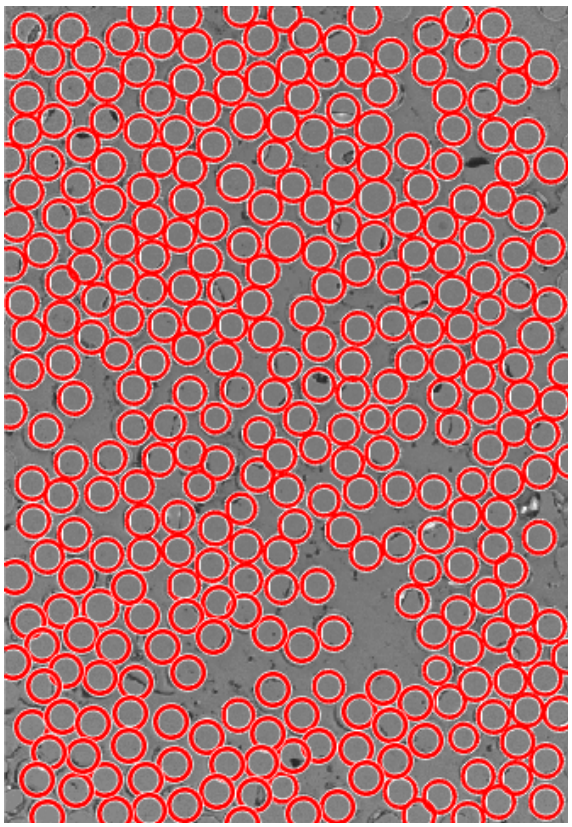

Figure 21: Micrograph of glass epoxy composite with fibers located in red.

Modulus

A water jet machine was used to cut one inch wide, ten inch long specimens out of the manufactured fiberglass plates, one of which is shown in Figure 20. One plate was cut along the fibers producing 0˚ coupons and the other plate was cut transverse to the fibers giving 90˚ coupons. To obtain the strain in the coupons during the tensile testing, quarter bridge strain gages were placed on the coupons (see Figure 22). Figure 23 shows the experimental setup for tensile testing of the coupons.

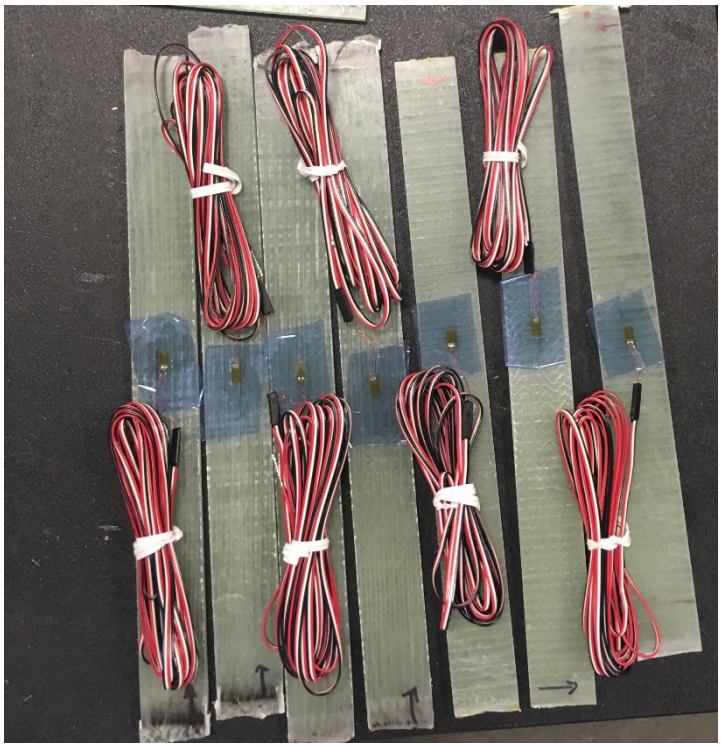

Figure 22: Tensile specimens with attached strain gauges.

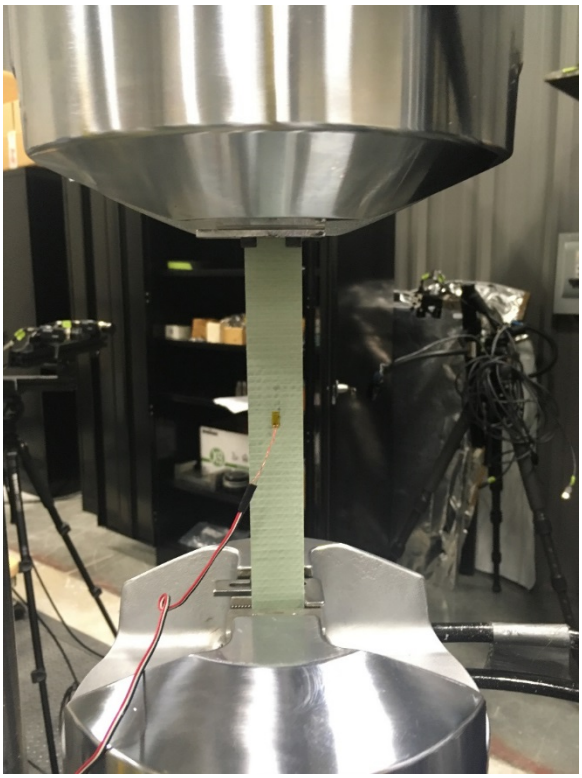

Figure 23: Tensile specimens were tested in a 22 Kip load frame.

Four 0˚ and four 90˚ tensile specimens were tested and the stress-strain plots of all 8 tests are shown in Figure 24. Taking the slope of the linear portions of the plots yielded the Young's moduli for the

coupons and these are displayed in Figure 25 and Figure 26. Table 6 displays the average moduli.

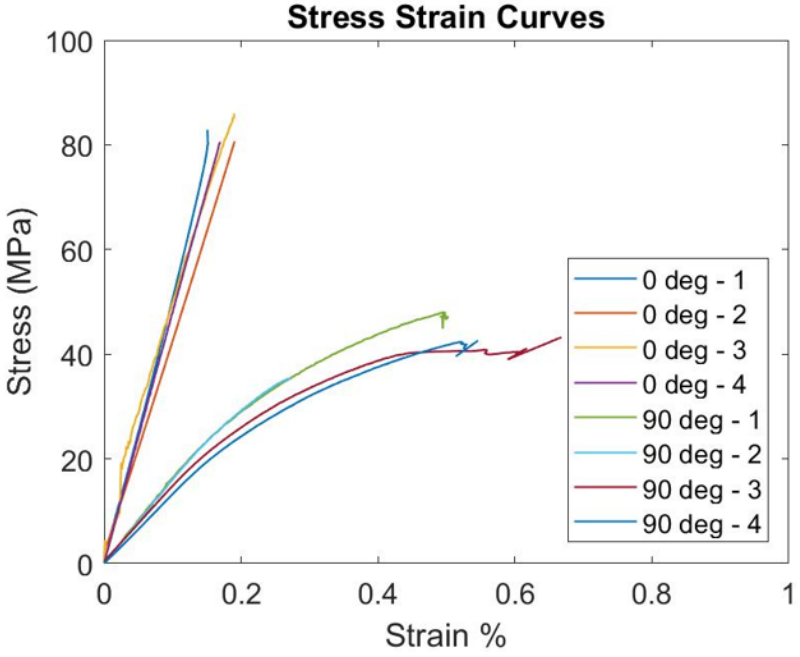

Figure 24: Stress-strain plots for all samples.

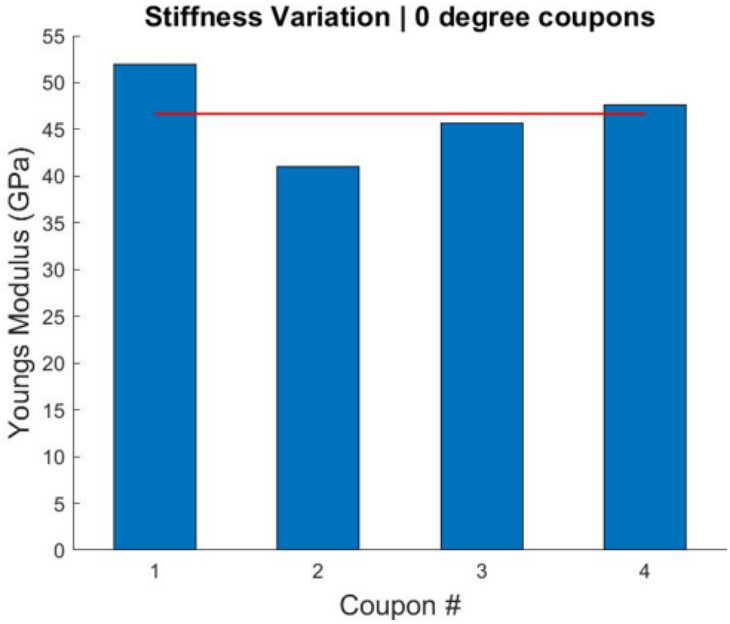

Figure 25: Young's Modulus for each of the 0˚ coupons.

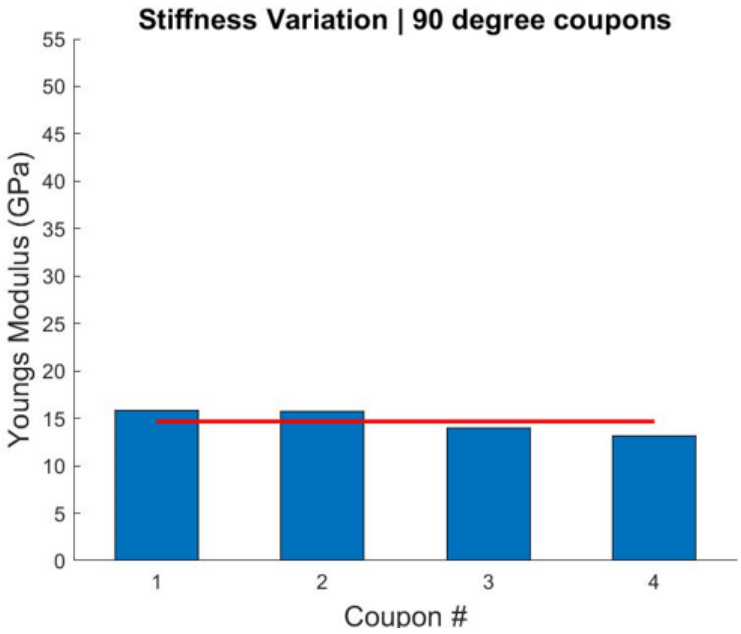

Figure 26: Young's Modulus for each of the 90˚ coupons.

Table 6: Measured Young's modulus data.

Parameter	Average Value
E_1	46.57 GPa
E_2	14.67 GPa

The glass modulus can be estimated by applying standard homogenization equations and backing out the glass modulus that must give the measured moduli, and :

$$E_1 = E_g V_g + E_r V_r$$

$$E_2 = \frac{E_g E_r}{E_g V_g + E_r V_r}$$

Solving this system of equations yields an estimate of 79.9 GPa for the glass modulus.

Coefficient of Thermal Expansion

The experimental method for measuring the in-plane coefficients of thermal expansion involved placing a small, 1"x1" square piece of cured composite inside a hot stage. The heating cycle consisted of holding at an initial temperature of 30˚C for 3 minutes and then ramping to 80˚C at 4˚C/minute. Once at 80˚C, the temperature was held for 5 minutes and then cooled back to 30˚C at a decreasing rate of 4˚C/minute. Digital Image Correlation (DIC) was used to analyze the strains in the sample during this heating cycle. Figure 27 shows the sample in the hot stage with the speckled pattern used as a reference for the DIC.

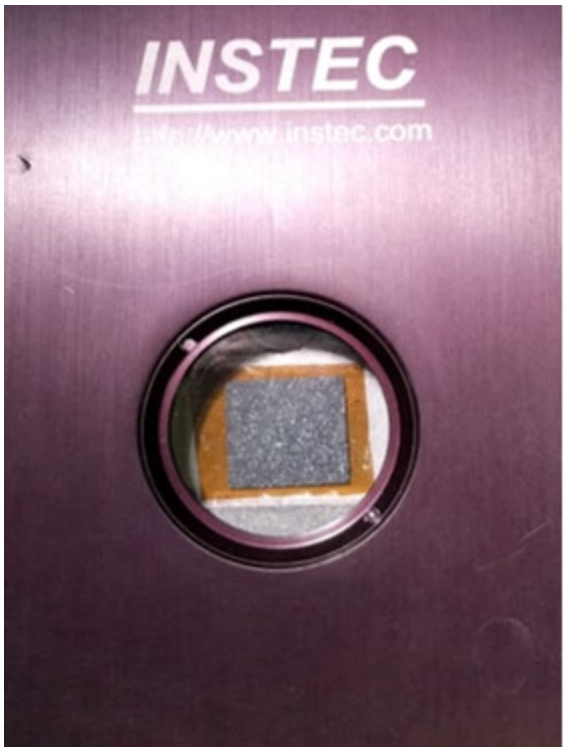

Figure 27: INSTEC hot stage with speckled composite sample.

A DIC camera was mounted just above the small window in the INSTEC hot stage. The images were analyzed using Correlated Solutions software to measure the full strain field of the sample for each image. The strains in the axial and transverse directions were averaged across the sample to get an estimate of the coefficients of thermal expansion in each direction. Figure 28 shows an image of the estimated strain across the sample for one point in time, and Figure 29 shows the average strain across the sample as a function of temperature and best fit lines. The results are listed in Table 7.

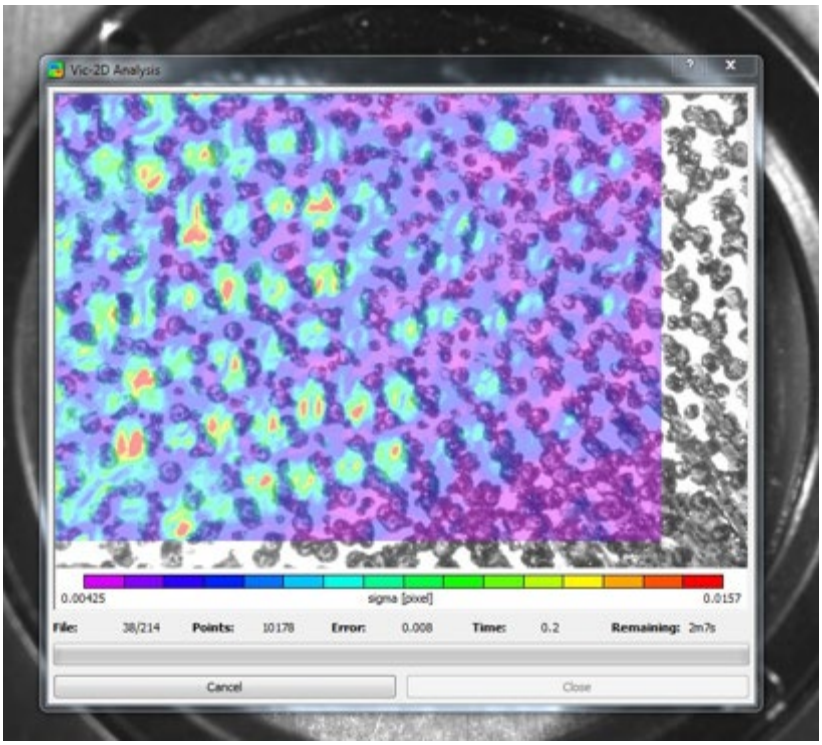

Figure 28: DIC analysis of the thermal strain across the specimen for one image.

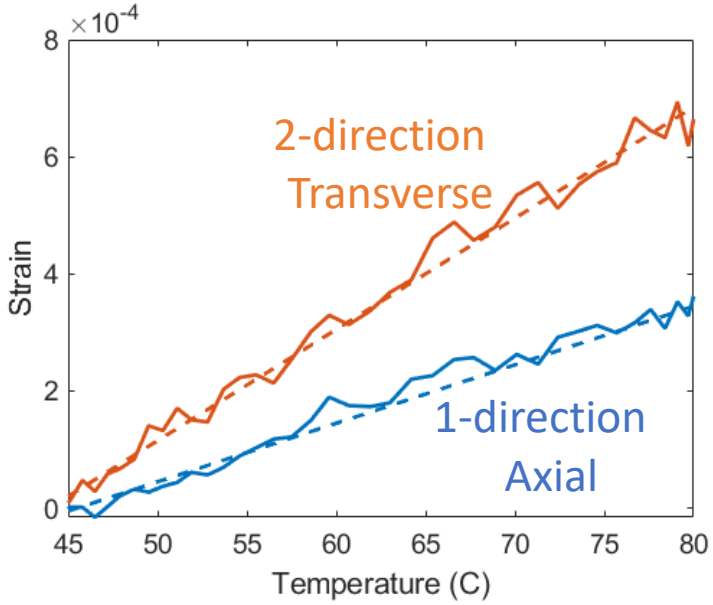

Figure 29: Average strain in the axial and transverse directions and linear best fit lines.

Table 7: In-plane CTE parameters.

Parameter	Value
α_1	12e-6 /°C
α_2	18e-6 /°C

Friction

Friction characterization was not in the initial scope of planned characterization tests. However, it was discovered that friction plays a critical role in the fiber buckling phenomenon of interest. In order to get a rough estimate of the frictional behavior, the coefficient of friction was measured between the mold (with mold release applied) and the cured part. A piece of cured composite was dragged across the mold using an MTS machine, and the force and displacement were recorded during the process. From there, the coefficient of friction was calculated. The coefficient of friction versus the displacement from the experiment is shown in Figure 30. Based on this measurement, the friction coefficient for the cured part in the mold was determined to be 0.1.

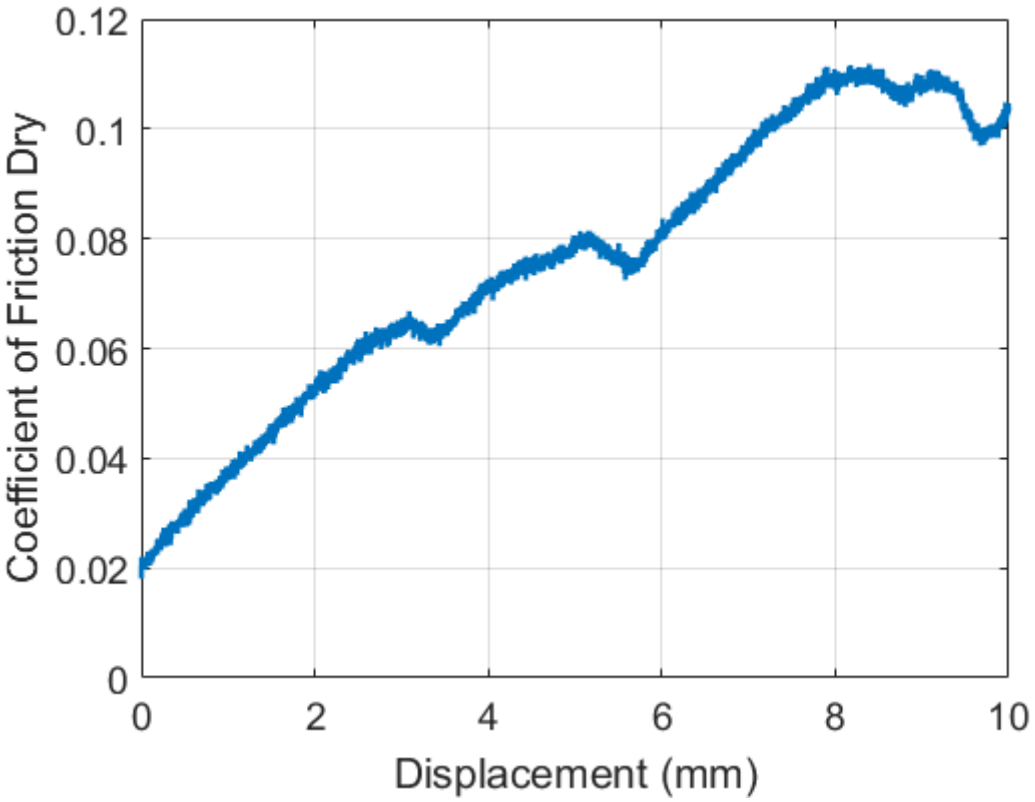

Figure 30: Friction coefficient between the mold and the cured part.

Since the resistive forces as a function of degree of cure are not known, a step function was used to model the frictional forces, with the coefficient of friction being equal to zero below the gel point of the resin and the coefficient of friction being equal to 0.1 above the gel point, as shown in Figure 31.

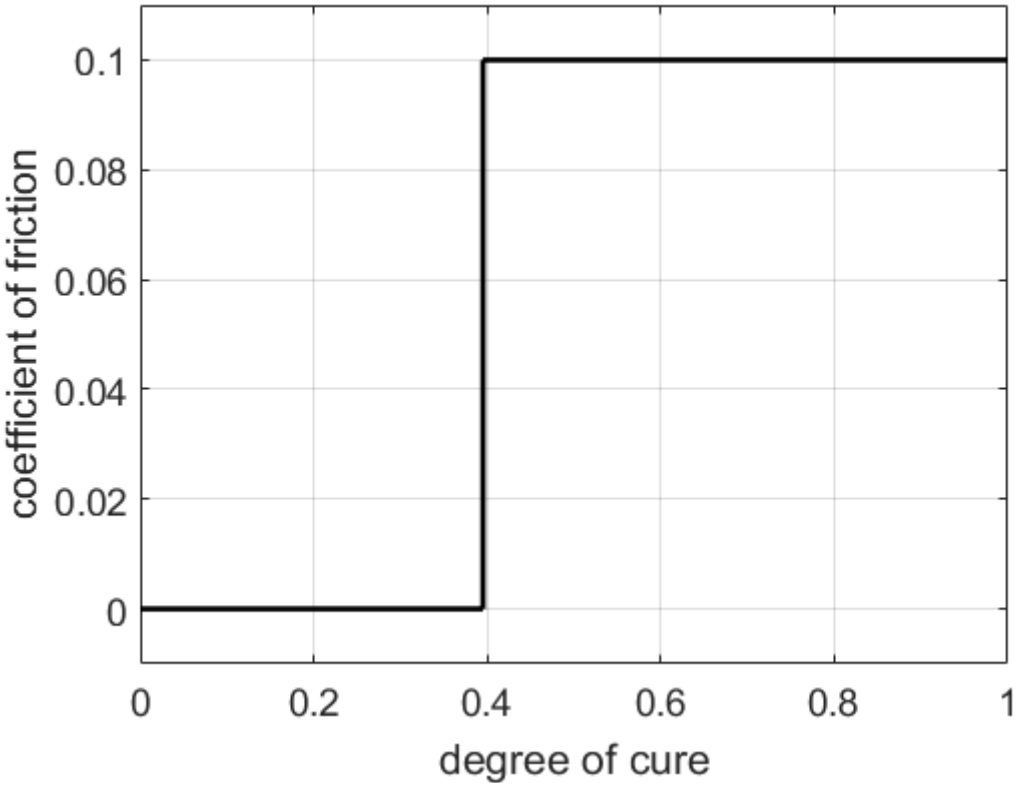

Figure 31: Given the absence of experimental data, a simple step function was used to model the onset of friction.

5.1.4 Lab Scale Experiment

A lab scale instrumented experiment was performed to provide experimental data and allow for greater observation and insight to the manufacturing process. Initially it was intended that the experiment would be used to reproduce the fiber buckling phenomenon of interest. However, the results of the simulation work showed that the compressive forces on the fibers, which cause buckling, scale with the size of the part, so fiber buckling cannot be replicated at lab scale. With that being said, the lab scale part is still useful to validate simulation predictions of flow, cure and compressive strain. What cannot be easily replicated in the lab is the magnitude of the compressive stress that arises from the full length of the spar cap. However, once the simulation tools are validated on the lab scale, they can be scaled-up to model the same physical phenomenon on the larger, spar-cap scale.

Materials and Methods

The lab scale part that was infused is flat and has dimensions of approximately 560 mm by 400 mm by 20 mm, which corresponds to approximately 1/100 length, full width, and ½ height compared to full scale spar cap dimensions. The mold was created by infusing unidirectional glass with resin. The glass and resin systems were the same materials used in the full scale spar cap. The temperature of the underside of the mold was controlled using 6- 1000 W hot plates, as is shown in Figure 32. Mold release was applied to the mold, and tape was applied around the edges, as shown in Figure 33. Pre-cut glass fabric pieces were then layed up on the mold. A LUNA fiber-optic strain sensor and several thermocouples were embedded in various locations throughout the part during manufacturing, shown in Figure 34.

Figure 32: Hot plates used as heating elements for the mold.

Figure 33: Mold release and sticky tape applied.

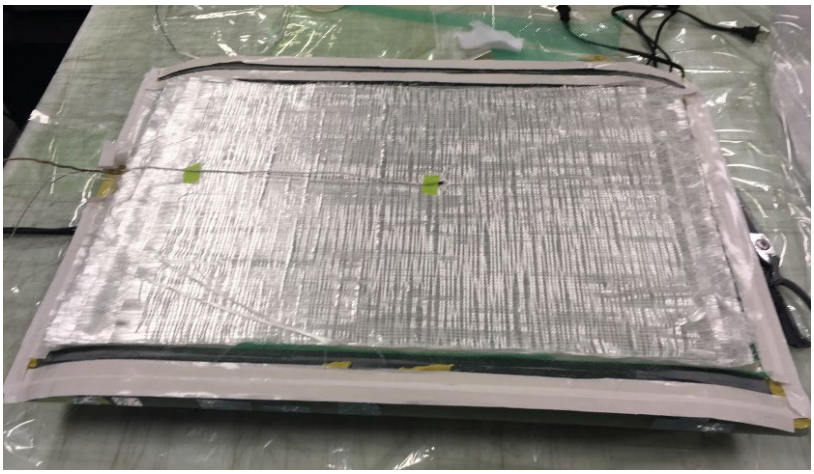

Figure 34: Glass fabric layed up with instruments embedded at select locations.

The LUNA fiberoptic sensor was placed on top of the bottom layer of glass, running down the center of the mold parallel to the glass fabric direction. Two thermocouples were placed near the LUNA sensor along the width and at distances of 50 and 280 mm along the length. A schematic of the LUNA sensor

and thermocouple placement locations is shown in Figure 35. A third thermocouple was added in the center of the mold below the top layer of glass (this thermocouple can be seen in Figure 34).

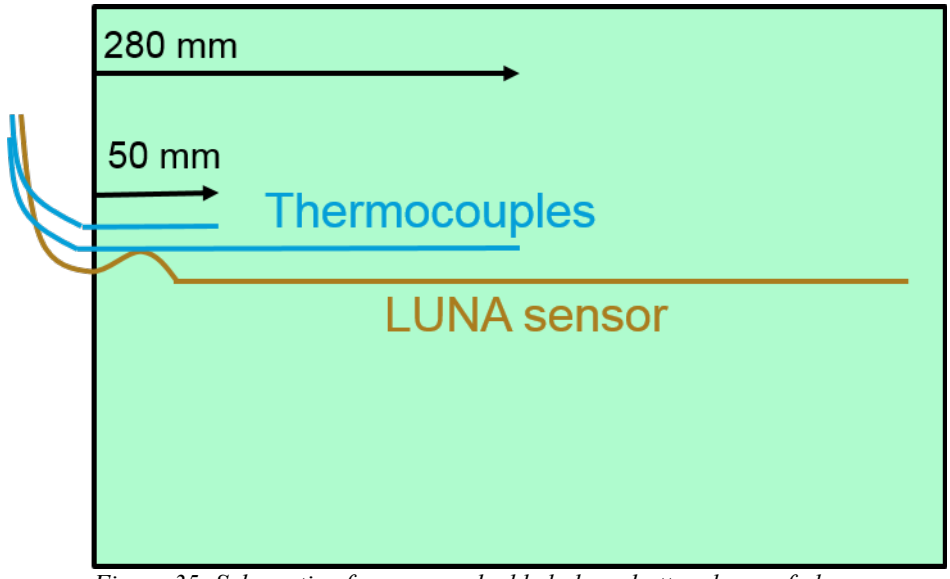

Figure 35: Schematic of sensors embedded above bottom layer of glass.

After the glass layup was finished, the infusion process was prepared using the same method as the real manufacturing process with the exception that no omega tubing was employed to flow the resin along the length of the part. Omega tubing is used on large scale parts to speed up and help resin distribution along parts with large infusion areas. This was not necessary for a lab scale part, so the omega tubing was not used. The semi-permeable membrane (orange material in Figure 36) and transfer medium materials were obtained from TPI. All other materials including the peel ply, vacuum bag, breather, tape, and tubing, used similar but not exact materials. The vacuum/infusion process went as follows:

1. Apply heat without vacuum for 30 minutes.
2. Apply vacuum and maintain heat for 30 minutes.
3. Begin resin infusion.
4. Maintain heat and vacuum for 3 hours.
5. Increase heat and maintain vacuum for 1.5 hours.
6. Turn off heaters; maintain vacuum until the part has reached room temperature.

At this point, the part was removed and the experiment was concluded.

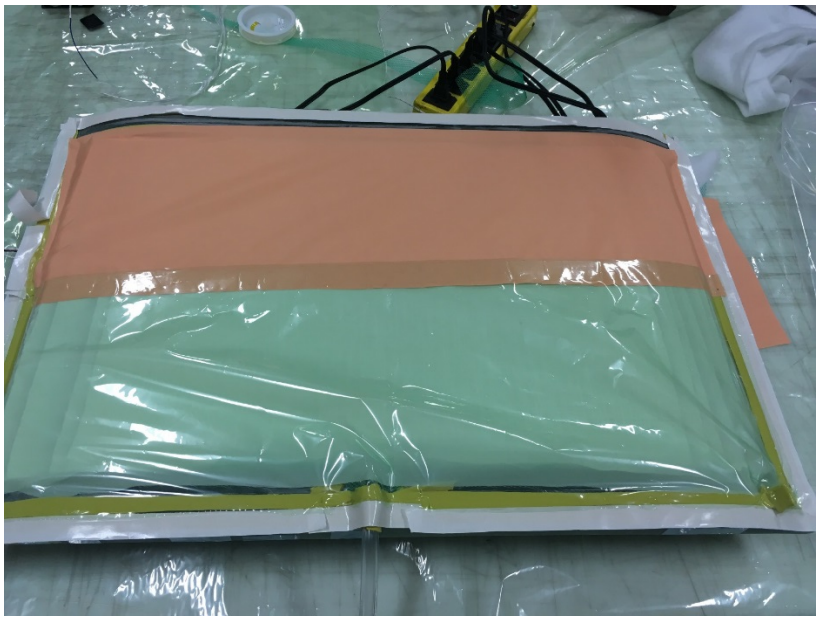

Figure 36: Part with first layer of bagging applied (breather and a second vacuum bag will be applied around this).

Experimental Results

Figure 37 shows LUNA strain results across the length of the part for several different times in the process. The sensor experiences tensile strain during the manufacturing process, but note that all of this strain is stress-free because it comes from Poisson's ratio and thermal expansion. A natural place to look for compressive stress in the fibers would be anything that prevents the fibers from straining freely. The two forces that work against fiber expansion are friction and (in the case of the full scale part) gravity. Friction was not originally considered, and this led to a brief friction study to provide an estimate of the maximum stress that can be induced in the fibers from friction.

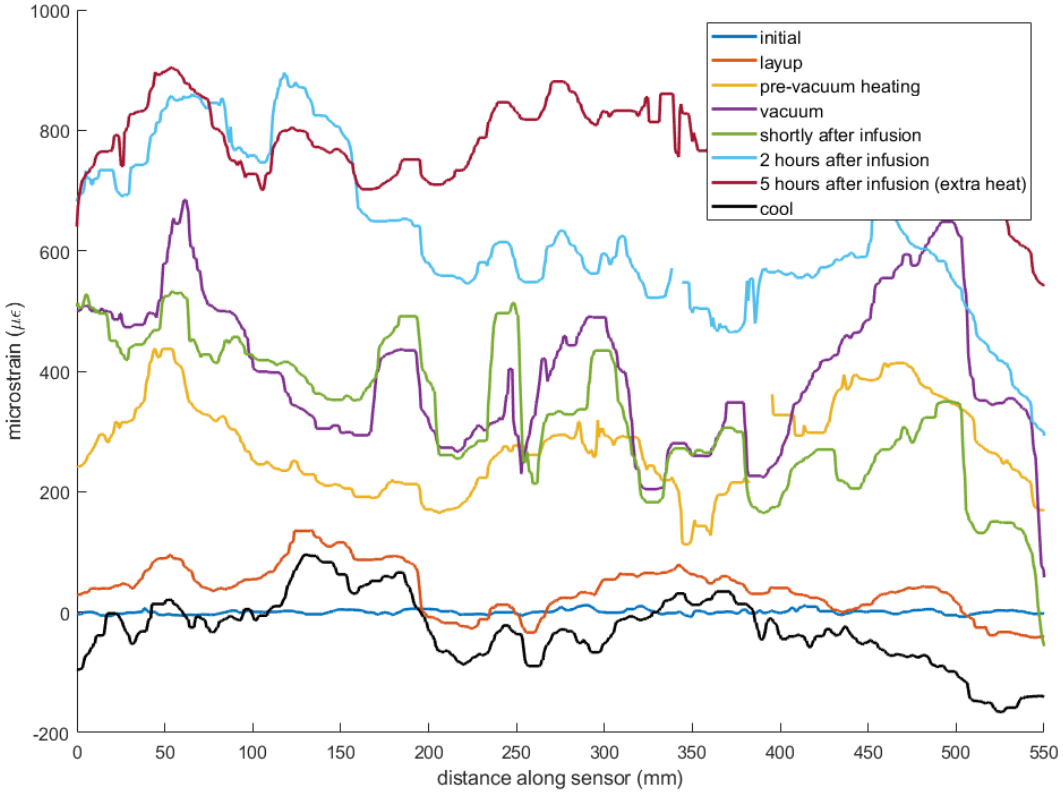

Figure 37: LUNA sensor results across the sensor for difference times.

The resistive force on the glass trying to expand is likely complex and viscous in nature while the resin is liquid. The force then becomes dry friction when the resin is fully cured, and it likely goes through a transition as the resin moves from liquid to solid. This appeared to be critical to capturing the physical process by which buckling of the fibers occurs. Therefore, a simple study was performed (shown in the material characterization section) in the project, with an understanding that more detailed study of this phenomena is needed in any extension of this work. While we planned to recreate fiber buckling with the lab scale part, friction scales with the size of the part and decreases the compressive forces in the glass. Therefore, the fiber buckling could not be recreated.

The LUNA and thermocouple results from the lab scale test can be compared to expected results calculated from CTE measurements. The experimental temperatures multiplied by the measured CTE values provides a prediction of strain for the part. This predicted strain can then be compared to the experimentally measured strain from the LUNA system. Figure 38 shows the LUNA sensor results through time at the same locations that thermocouple measurements were made. The times of the different process steps are also labeled. Figure 39 plots the LUNA result through time at 50 mm along the sensor compared to the result using the measured temperature at that point and the CTE. The results match closely, suggesting that the fibers are not being prevented from expanding. Figure 40 shows the same results but at 280 mm along the sensor (halfway through). In this case, the LUNA results are lower than the predicted result based on CTE, suggesting that there are forces preventing the fiber in the center of the part from expanding freely. If we estimate the difference in strain from the friction forces shown in Figure 31, we only predict a difference in strain of 30 microstrain, compared to the 100-200 microstrain we measured with the Luna system, suggesting that further work is needed to accurately model frictional forces.

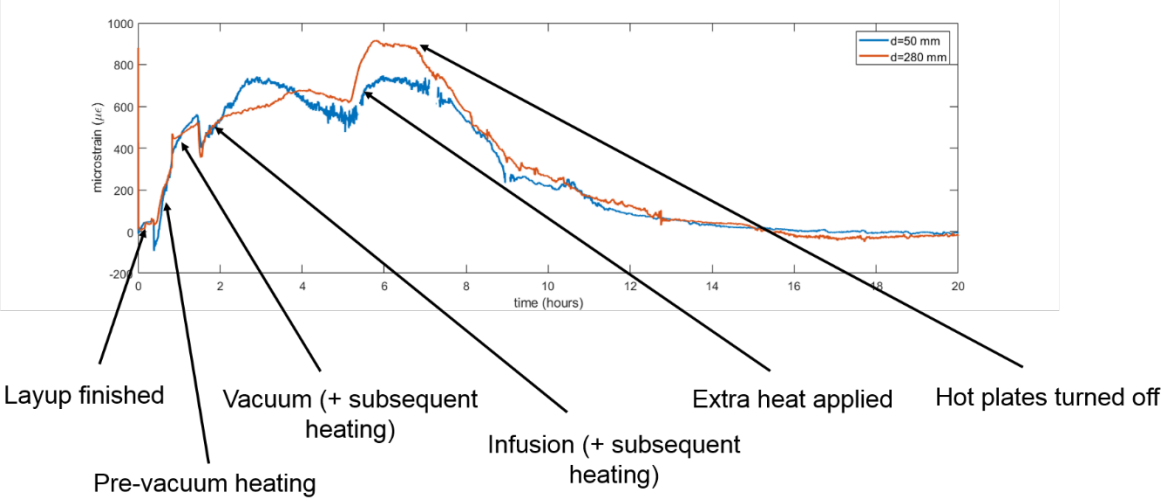

Figure 38: Time history of LUNA results at thermocouple locations with process steps labeled.

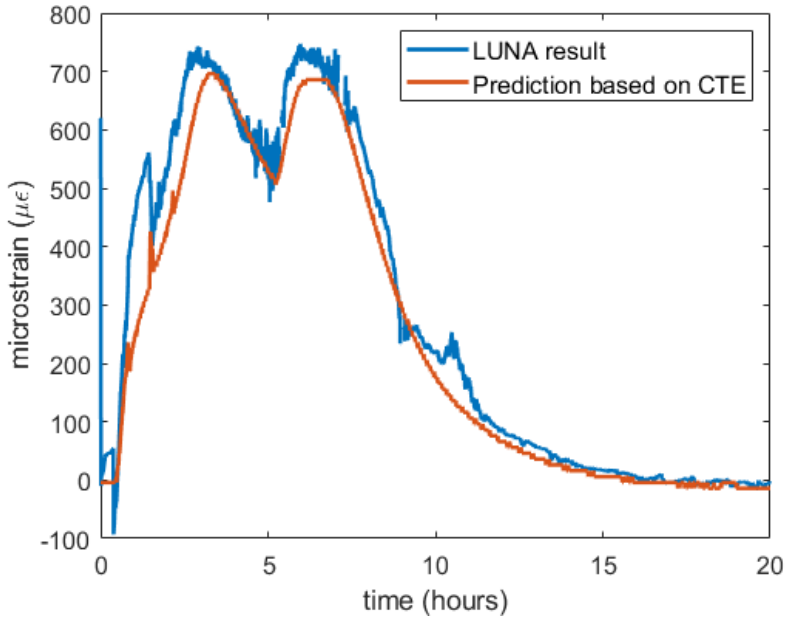

Figure 39: Comparison of measured result to predicted result at 50 mm along fiber.

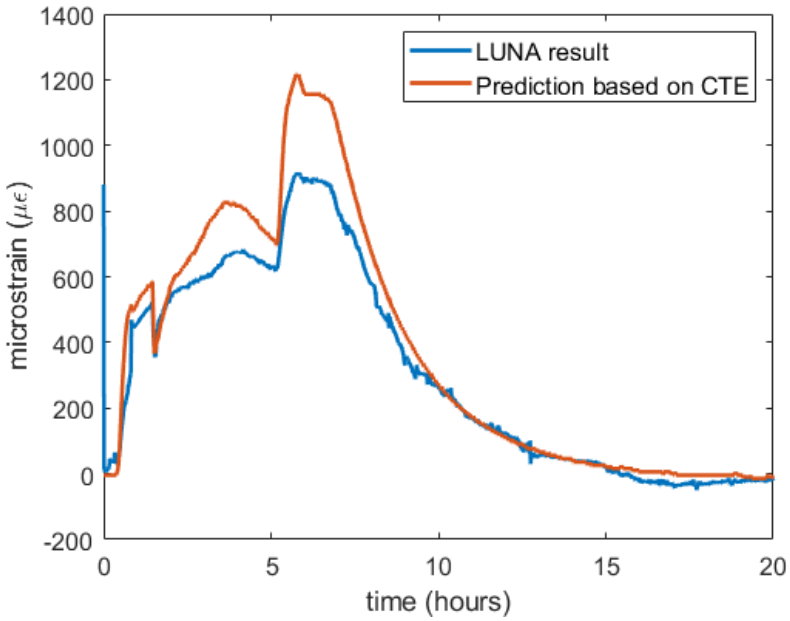

Figure 40: Comparison of measured result to predicted result at 280 mm along fiber.

5.2 Modeling and Simulation

The manufacturing process of the spar cap infusion was modeled using a non-isothermal filling simulation in PAM-RTM to capture the heat transfer and cure kinetics while the resin infuses the spar cap. Once the resin finished infusing, the temperature and degree of cure information were imported into an ABAQUS model, where the heat transfer and cure kinetics modeling continued in a coupled stress-temperature model.

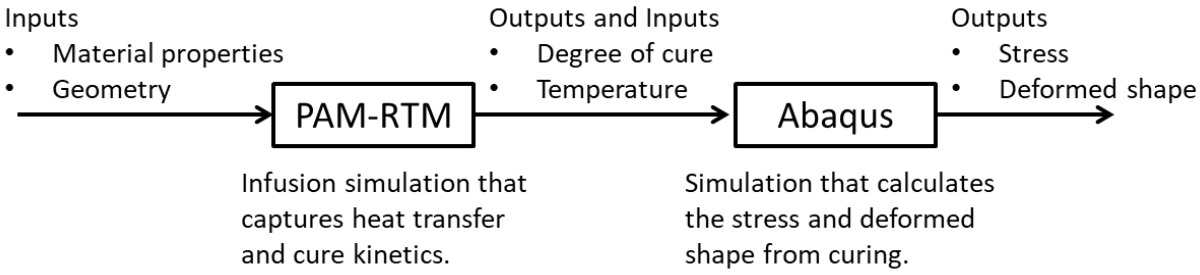

Figure 41: Flow block diagram showing inputs and outputs for simulation method

5.2.1 PAM-RTM Model

In order for the PAM-RTM model to run efficiently, a few adjustments were made to the spar cap geometry. First, the feathering of the geometry at the edges was eliminated to simplify mesh issues and improve run times. Secondly, the tubing, transfer medium, and tool elements were combined into one part because the small size of the transfer medium and tubing caused meshing them explicitly to be untenable. The combined part was treated as resin permeable, so that it could model the infusion of the transfer medium and tubing. The porosity of the combined part was given such that it accurately represented the porosity of all parts. Inlet pressure of ambient pressure was applied at 20 m down the longitudinal axis of the spar cap (as is the case in the actual spar cap) and vacuum applied along the center line of the top of the part. These conditions are described in Figure 42.

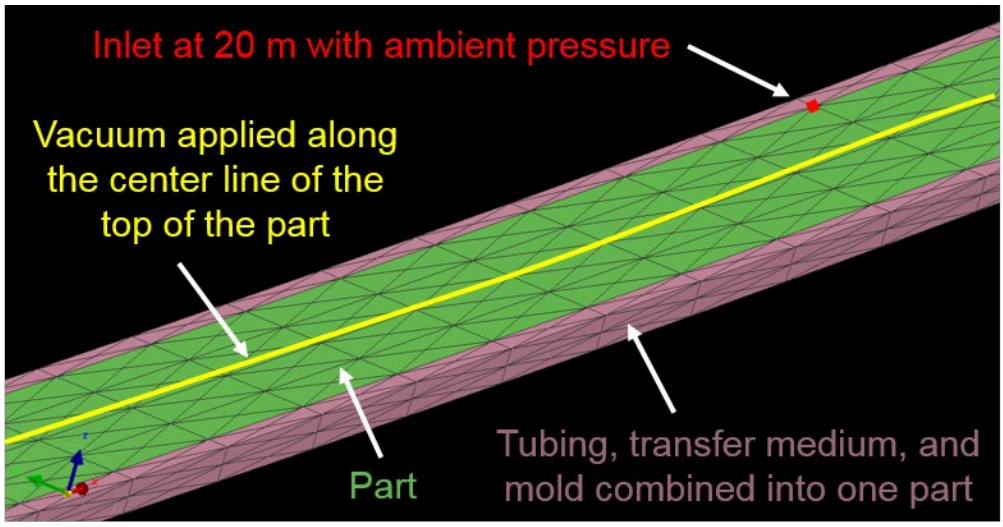

Figure 42: Overview of PAM-RTM model.

5.2.2 PAM-RTM Results

Figure 43 shows the filling time results with the time in units of seconds, the cooler colors mean that portion of the cross section filled faster than the hotter colors which had a slower fill time.. As is observed in the actual manufacturing process, the resin quickly flows down the length of the spar (through the tubing) and around the bottom (through the transfer medium) then slowly fills towards the top center.

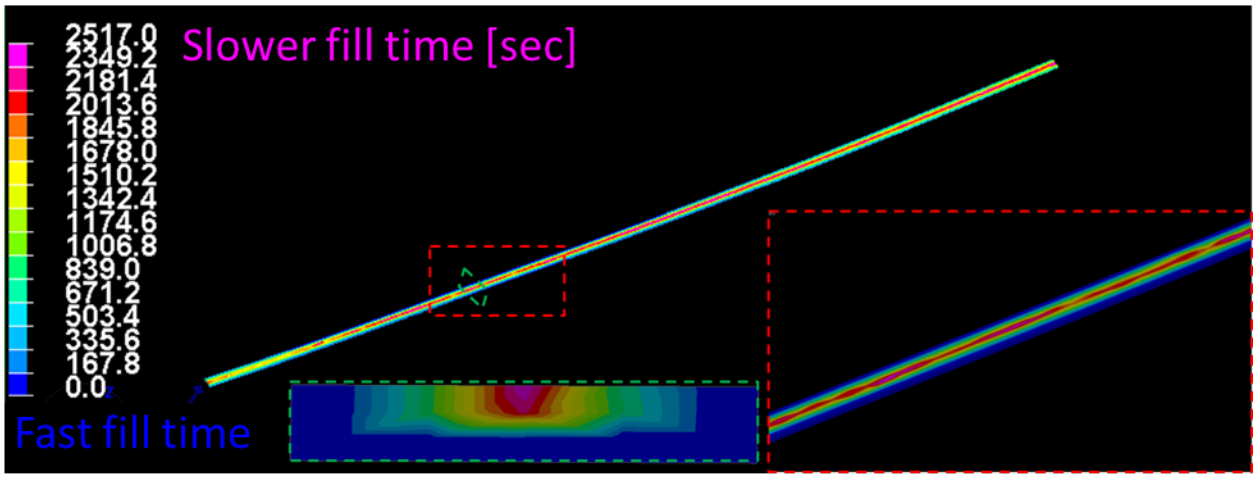

Figure 43: PAM-RTM fill time results.

Figure 44 shows the material age of the resin in the fully infused part, which corresponds to when the resin at each location entered the part. As would be expected, the resin near the inlet is the "youngest" resin and the resin at the edges is the "oldest" resin. Also note that the resin on the vacuum side is significantly older than the resin on the infusion side, particularly near to the infusion point.

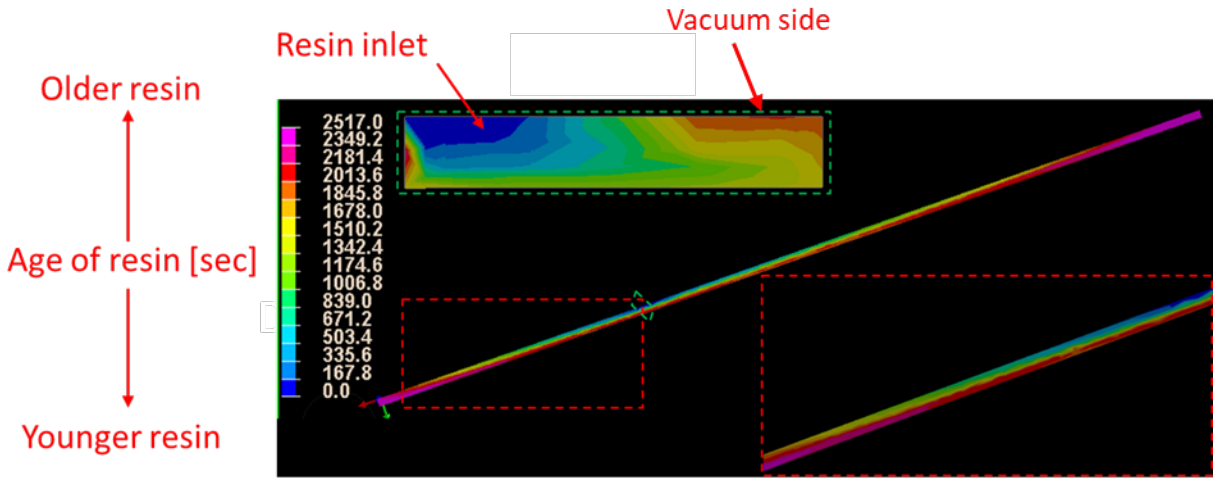

Figure 44: PAM-RTM material age results.

Figure 45 shows the degree of cure of the resin at complete fill. Note that the resin essentially tracks with the material age result. This makes sense because the resin that has been in the part longer has had a longer time to cure.

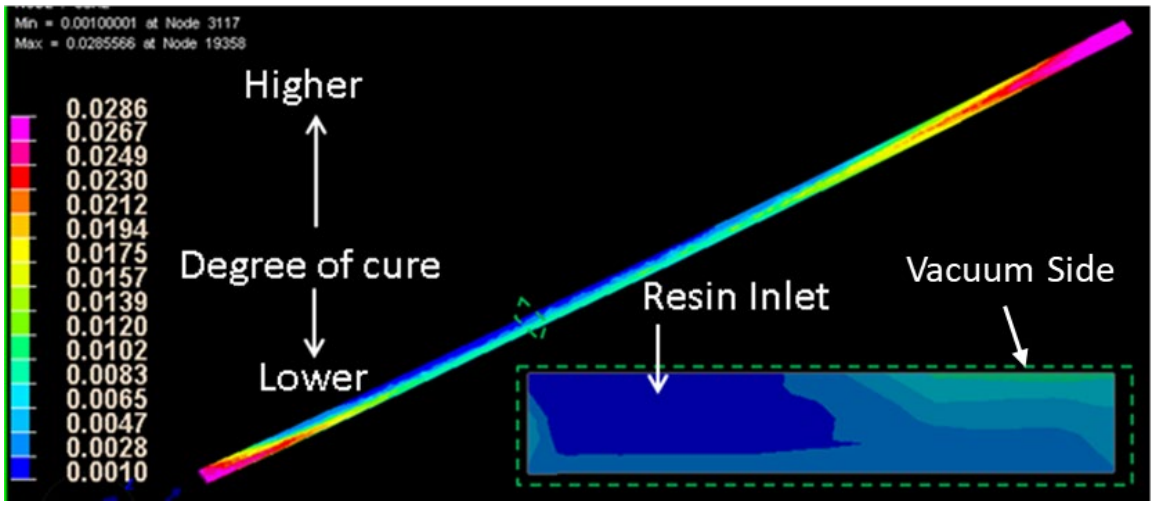

Figure 45: PAM-RTM degree of cure results.

Figure 46 shows the temperature in the part at complete fill. The temperature also roughly tracks with the material age and degree of cure. This make sense because the resin releases heat during the cure process. Note that the resin is still largely uncured (maximum degree of cure of roughly 3%) when the infusion is completed. However, this does not mean that the difference in cure is trivial. As the exothermic cure increases the temperature, which increases the cure rate, the reaction is autocatalytic. The resin which is at 3% cure may not be significantly more cured than the resin which is uncured, but it is still 30-40 minutes ahead in the cure process, therefore when the resin at the end of the part reaches a temperature where the cure rate increases significantly, there will be a large discrepancy in degree of cure values.

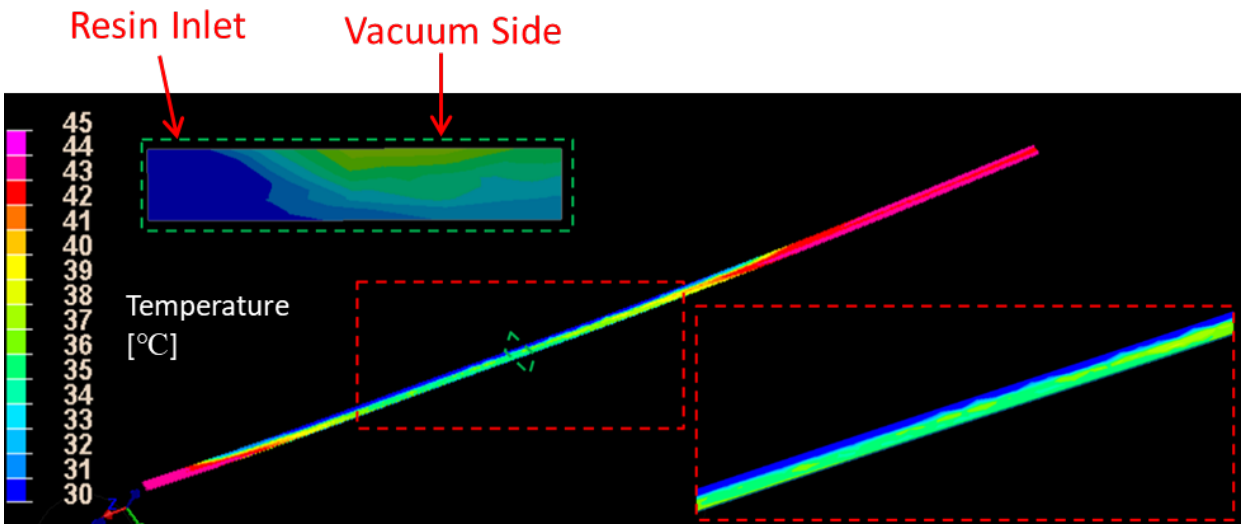

Figure 46: PAM-RTM temperature results.

5.2.3 ABAQUS Model

The ABAQUS model geometry for purposes of heat transfer and cure kinetics modeling to predict stresses and displacements in the part was exactly the same as the PAM-RTM geometry. In this case, the combined mold/transfer medium/tubing part is treated just as the mold. A shell mesh was used to enable the model to run quickly enough for a transient solution to be feasible and to prevent numerical issues that arise in the solid model surface contact. The boundary conditions applied to the model were atmospheric pressure along the top surface of the part, gravity everywhere, and isothermal boundary conditions with the top surface of the part at room temperature and the bottom surface of the mold at 35 C. The mold was held completely fixed and the part was held fixed in the transverse direction and was given a surface contact with the mold. The surface contact friction was applied depending on the degree of cure according to Figure 31. Cure shrinkage was also applied to the model. The initial temperatures and degrees of cure were imported from the end result of the PAM-RTM model. Figure 47 and Figure 48 provide a schematic and shows the model with its applied loads and boundary conditions.

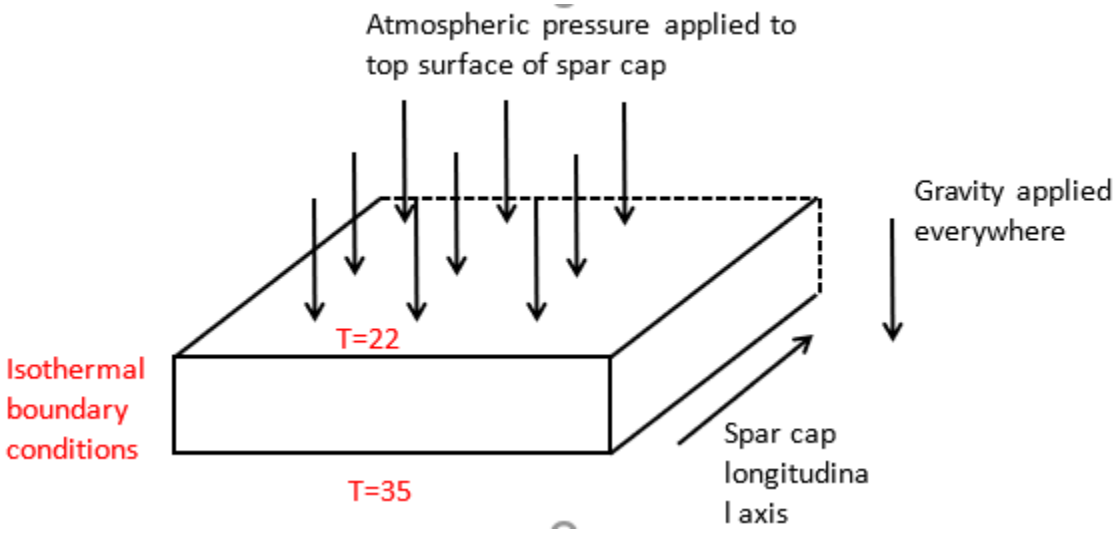

Figure 47: Schematic showing application of mechanical and thermal boundary conditions

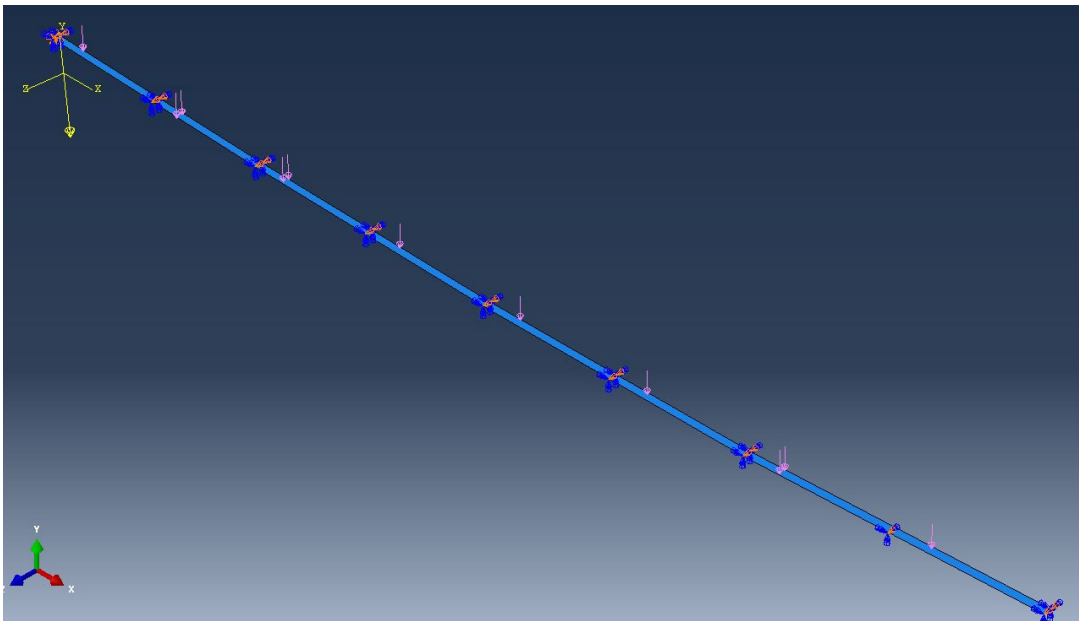

Figure 47: Loads and boundary conditions for ABAQUS model.

5.2.4 ABAQUS Results

Figure 49 shows the stress in the fiber direction at the beginning of the analysis. This is before any expansion or contraction takes place, so this stress is purely from the force of gravity and Poisson's effects. The results show gravity puts around 1 MPa of compressive stress on the homogenized section that is in the top (middle) of the part.

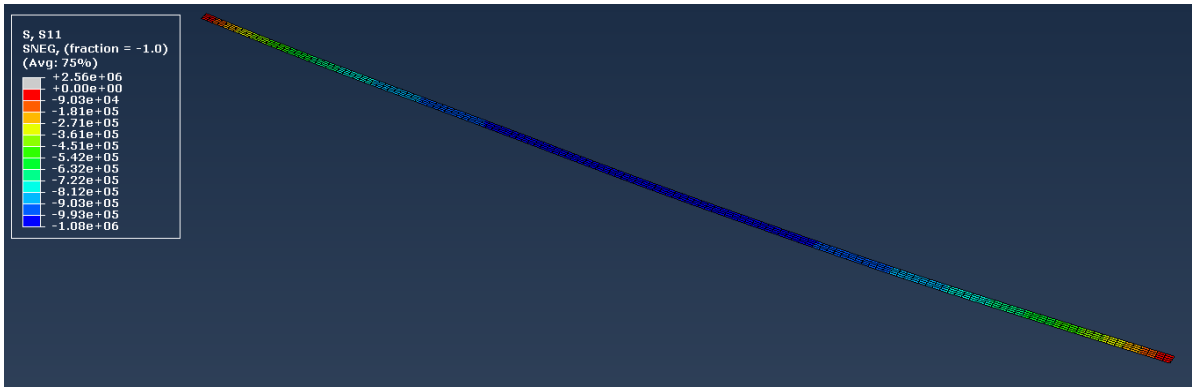

Figure 48: Stress in the part from gravity.

After roughly 100 minutes of curing, the resin has reached a point where the edges of the part have passed the gel point but the center, near the infusion point, is still liquid. Figure 50 shows the degree of cure of the resin at this time and Figure 51 shows a map of the friction coefficient, where the red areas represent resin that has passed its gel point and the blue areas represent resin that has not yet passed its gel point. Because of the friction that is applied to the model in these regions, any increase in temperature in the center of the spar cap? will be resisted by frictional forces. Figure 52 shows the homogenized stress at 100 minutes. Figure 53 shows the stress resulting from cure shrinkage in the fibers. Note that the stress in the fibers from cure shrinkage is very small where the compressive stress is large in the part. This is because the stress from cure shrinkage is very small until after the resin gels.

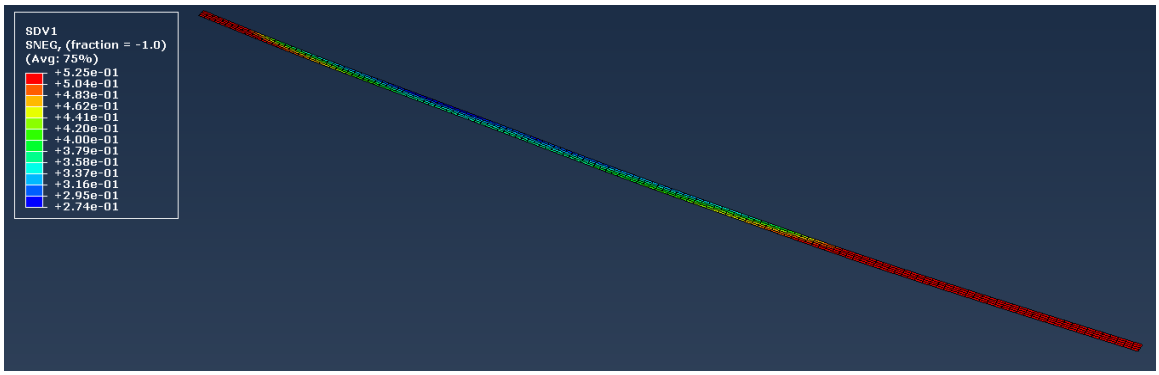

Figure 49: Resin degree of cure at 100 minutes.

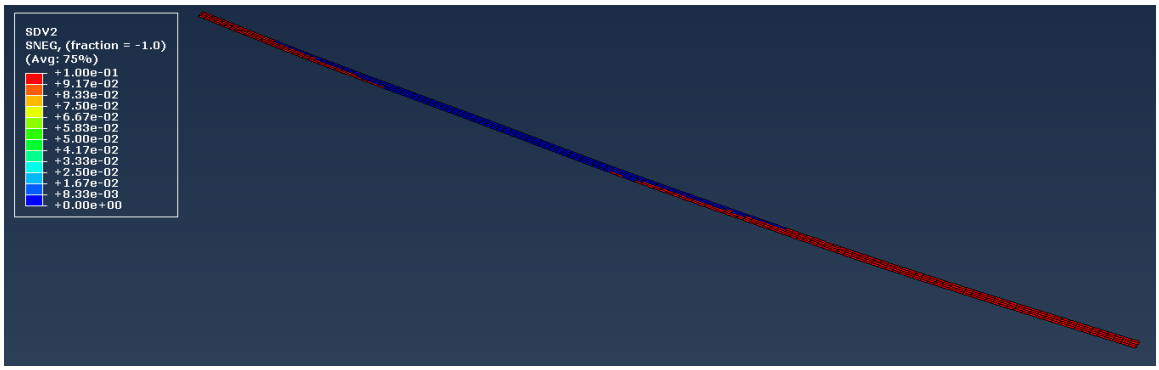

Figure 50: Map of where resin has gelled at 100 minutes.

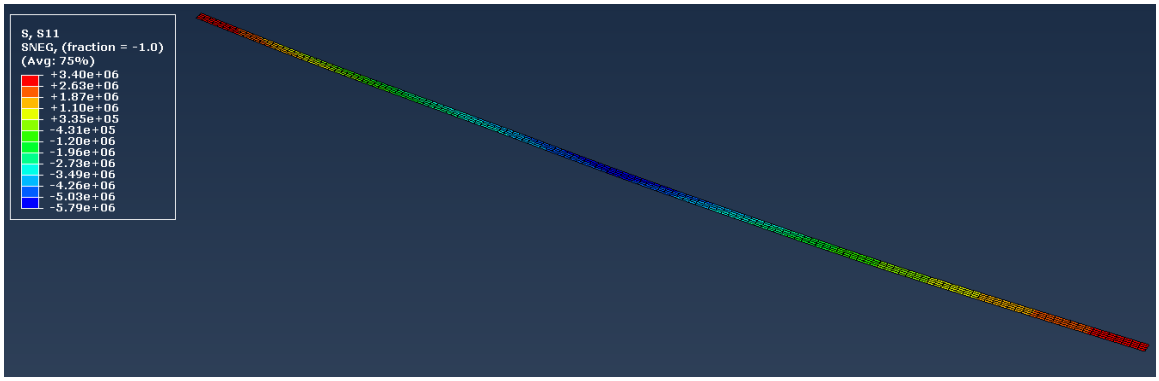

Figure 51: Stress in homogenized part from gravity and friction at 100 minutes.

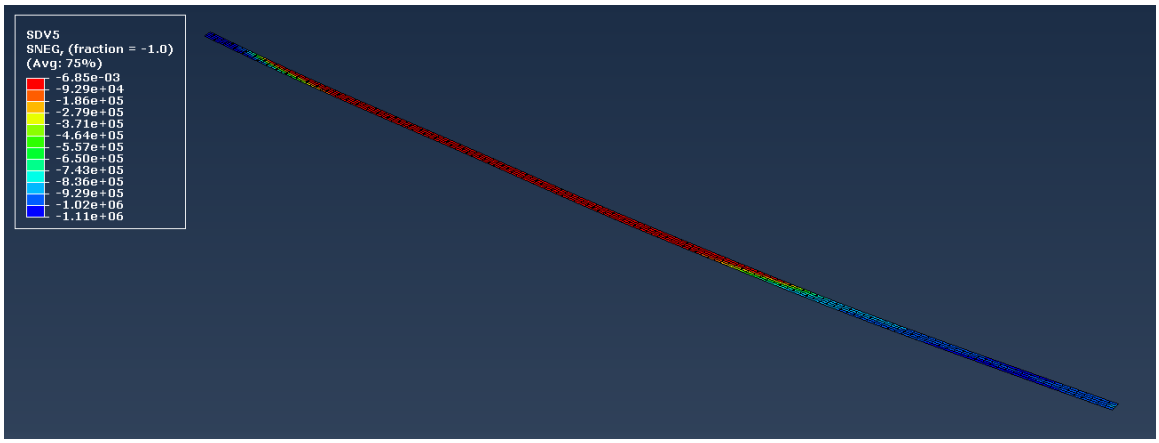

Figure 52: Stress in the fibers from cure shrinkage at 100 minutes.

In order to estimate the overall stress in the glass fibers, the homogenized stress coming from gravity and friction is divided by the fiber volume fraction and then the stress coming from cure shrinkage is added to that value. Figure 54 shows the resulting fiber stress. This result shows through comprehensive process modeling that a source of significant compressive stress in the fibers can be introduced from this manufacturing process, which was the ultimate goal of this project.

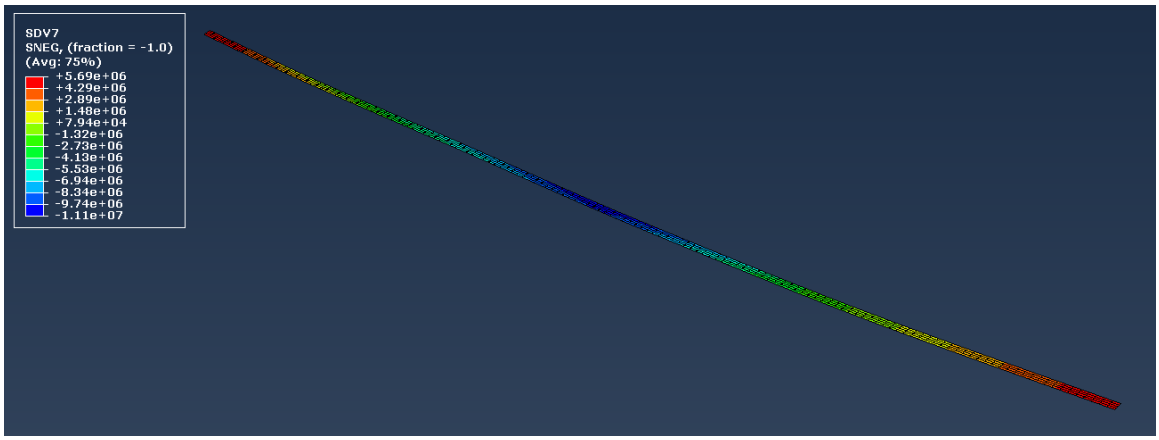

Figure 53: Total stress in the fibers at 100 minutes.

6. BENEFITS ASSESSMENT

The results of the work described in this report demonstrate that simulations can be used to capture and identify manufacturing problems encountered in the VARTM process for wind turbine spar caps. In addition, simulations can be used to develop a solution to the manufacturing problem instead of an expensive trial and error method. The implementation of simulation into the development cycle of new components, material systems, or manufacturing processes could save companies like TPI money by predicting manufacturing issues before they occur or optimizing the current manufacturing method to reduce cycle time as much as possible.

In addition, this simulation work revealed that the difference in material age (when the material was introduced into the part) causes differences in the cure history along the length of the part. This in turn causes friction forces to develop that prevent stress-free thermal expansion of fibers in the center of the spar

cap. The compressive stress that develops from the frictional forces as well as gravity cause the fibers to buckle.

7. COMMERCIALIZATION

These results have shown that simulation can be used by composite manufacturers to capture physical phenomena present during manufacturing in order to identify causes of defects or optimize the manufacturing process.

8. ACCOMPLISHMENTS

This project showed the merits of using simulations to assist in understanding of manufacturing processes and problems.

1. Resin properties were measured in the lab at the CMSC, including cure kinetics, viscosity, modulus, and chemical shrinkage.
2. Glass properties measured in lab were permeability of the glass fabric and modulus.
3. The composite properties measured were fiber volume fraction, modulus, coefficient of thermal expansion, and friction.
4. A lab scale spar cap section was manufactured in house to recreate the fiber buckling defect albeit unsuccessfully.
5. A PAM-RTM simulation was performed to capture the heat transfer and cure kinetics of the infusion process on the spar cap.
6. An Abaqus model was linked to the PAM-RTM results to recreate the stress and displacement associated with further heat transfer and curing of the part.

9. CONCLUSIONS

Wind blade spar cap manufacturing utilizing resin transfer molding is a time consuming process and the largest bottleneck in the throughput of spar caps is waiting for the infused resin to cure. Because of buckling which has been observed in parts which are cured too quickly, TPI intentionally slows the cure process down significantly to prevent quality issues. Phase I of this project resulted in a physics-based model which simulates infusion, heat transfer, cure kinetics, and stress-deformation. The material parameters of the spar cap materials were measured during Phase I and the parameters were populated into the model. The results of the model showed that the spar cap infusion strategy creates a scenario where the resin that will ultimately be towards the ends of the blade infuses first and the resin that will be in the middle of the blade infuses last. This creates a situation where the resin in the middle of the blade is the last to develop modulus. Some preliminary experiments showed that friction between the spar cap and the mold begins to develop once the part is cured and that a point can be reached where the maximum amount of frictional force can be significant while the center of the spar cap is still heating up from cure exotherm. This heating will cause expansion of the fibers, and when the frictional forces prevent the fibers in the center of the blade from expanding a significant compressive force is introduced which can cause the fibers to buckle.

A PAM-RTM model and Abaqus model were linked and showed that the difference in material age leads to a significant difference in cure history throughout the part. In fact, the ends cure several minutes before the center of the spar cap. When the ends cure, frictional forces that resist thermal expansion of the fibers in the center begin to develop. As the center is still curing and increasing in temperature, a significant compressive stress is introduced into these fibers. The resin is still in a liquid state and does

not reinforce the fibers. The only thing preventing the fibers from buckling is the pressure of the vacuum bag. Simulation results suggest that the stress introduced from friction is the largest source of compressive stress in the fibers, the stress from the weight of gravity is significant but secondary, and the compressive stress from cure shrinkage does not play a significant role in the buckling of fibers. Some aspects of the model are still low in fidelity, so while this model shows the mechanism by which compressive forces are introduced, more work needs to be done before it could predict whether or not a buckling event would be likely to occur given a set of manufacturing conditions.

10. RECOMMENDATIONS

Incorporation of simulation software in the design process of parts and manufacturing cycles can prevent costly manufacturing mistakes. However, the material system must be characterized prior to simulation, and the simulations must be validated before they can be used to optimize or predict the manufacturing cycle.

11. REFERENCES

Castro, J. M., & Macosko, C. W. (1982). Studies of mold-filling flows in the reaction injection molding process. *AICHe J.*, 250-260.

Darcy, H. (1856). Les Fontaines Publiques de la Ville de Dijon. Paris: Victor Dalmont.

DiBenedetto, A. T. (1987). Prediction of the glass transition temperature of polymers: A model based on the principle of corresponding states. *J. Polym. Sci. PartB: Polym. Phys.*, 1779-2038.